

Conceptual Design Report for Diamond Anvil Cell Setup (DAC) at the HED instrument of the European XFEL

(funded and developed in the frame work of the HIBEF project)

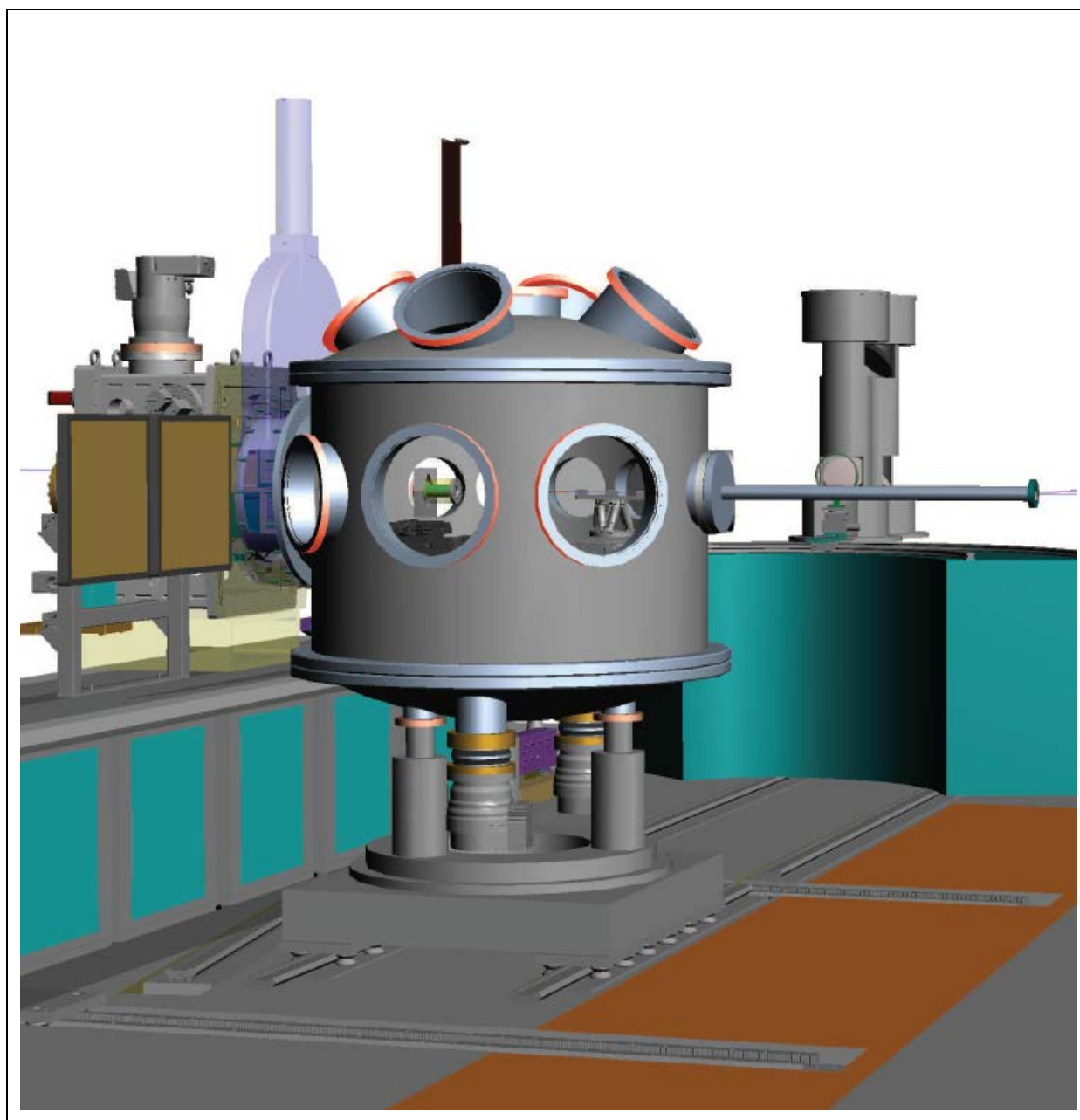
by

H. P. Liermann (editor)

with contributions by

H. Damker, Z. Konôpková, K. Appel, A. Schropp, S. McWilliams, A. Goncharov, C. Baehtz

(Ver_2_5, 12/10/2016)



3D representation of the DAC setup at the HED instrument of the European XFEL. The dynamic DAC with sample stack is located in a vacuum chamber. The vacuum chamber is positioned on a manual rail system to move the DAC setup in and out of the beam. The detector bank downstream from the chamber holds an AGIPD 1 M and two PE XRD 4343 ct for the detection of diffraction images. The detector bank is fully motorized. Behind the DAC vacuum chamber is indicated the position of the diffractometer for pulsed magnetic studies also positioned on a manual operating rail system.



Content

1. Introduction	4
2. Scientific Goal and Ideas using DACs at the European XFEL	6
2.1. Study of phase properties and EOS at pressures and temperatures of the interior of extra-terrestrial planets	7
2.2. Compression rate dependence of physical properties	11
2.3. Exploring stellar interiors and fusion under WDM conditions in the isochoric heated DAC	12
2.4. Thermal properties (thermal diffusivity) of mineral and melts at earth and other planetary core conditions	13
2.5. Study of early stage of melting and crystallization via phase contrast imaging (PCI) and diffraction in normal and radial geometry	13
3. DAC techniques	15
3.1. Dynamic DAC	16
3.2. Double Stage DAC	17
3.3. Do we need the European XFEL and how would a dDAC/dsDAC experiment at the HED instrument be conceptually setup?	18
4. X-ray Beam Requirements and Expected Scattering Power	21
4.1. Bunch Structure of the European XFEL	21
4.2. CRL focusing (provided by HED)	22
4.3. Nano focusing (provided by Workpackage x-ray Instrumentation)	24
4.4. Scattering power	26
5. Diamond Anvil Damage thresholds	27
6. Sample Environment Requirements (Vacuum Chamber)	29
7. Sample Positioning Requirements	32
8. Sample Heating and Temperature Determination in the DAC	29
8.1. Isochoric Heating	33
8.2. Pulsed Infrared Laser Heating	34
8.3. Resistive Heating	35
9. Pressure Measurement in the DAC	32
10. Clean Up Slits (pinhole)	36
11. Beam Stop and Beam Transport after Sample	39
12. Detector Requirements and Instrumental Resolution	39



12.1. XRD a-Si Detectors from Perkin Elmer	40
12.2. JUNGFRÄU (adJUstiNg Gain detector FoR the Aramis User station)	41
12.3. AGIPD (Adaptive Gain Integrating Pixel Detector)	41
12.4. Instrumental Resolution	42
12.5. Detector Support System (together with Workpackage x-ray Instrumentation)	43
13. Control System, Instrumentation Specific Software and Implementation	45
14. Analysis Software for pressure and temperature measurements and x-ray diffraction	45
15. Preparation Laboratories	46
16. Summary of Combined Usage of Instrumentation within HIBEF project and HED instrument	46
17. Time line and first experiments	47
18. Summary	48
19. References	49
20. Appendix A	52



1. Introduction

Diamond anvil cell (DAC) have been for decades the choice of instrumentation for creating static (hydrostatic and non-hydrostatic) high-pressure conditions to simulate pressure and temperatures encountered in the interior of the earth or other extra-terrestrial planets. The technique has also been used extensively in high-pressure physics to investigate and verify the existence of novel compounds such as metallic hydrogen predicted by theory or other molecular solids as well as an effective tool for synthesis of new compounds.

Until a few years ago the limits of pressures and temperatures achievable have been around 400 GPa and 4000-5000 K on FeO, employing the laser heated diamond anvil cell (Tanteno et al. 2010), which are still heavily debated. However, the development of the so-called double stage Diamond Anvil Cell (dsDAC) has seen increase in pressure at room temperatures of up to 775 GPa (Dubrovinsky et al. 2015) and recently 1 TPa (Dubrovinskaia et al. 2016) with an upper limit not yet in sight. Unfortunately, due to the nature of the technique it has not been possible to reach high temperature at simultaneous high pressures with this technique. This is because of the usage of nano crystalline second stage diamonds that offer a very high defect structure and thus increased strength in comparison to regular single crystal diamonds. However, they are quickly losing strength during heating along with the loss of pressure. Thus, the idea is to get diffraction information from the sample at high-pressure before the defect structure disappears and pressure drops. This has been tried at 3rd generation synchrotrons with very limited success because of the lack of flux. We will show based on initial simulations that the flux available at the HED instrument of the European XFEL will be sufficient to collect multiple one-shot diffraction images at the maximum repetition rate of the XFEL of 4.5 MHz over a single infrared heating pulse of up to a 1 μ s, enabling the collection of an entire high-pressure and –temperature equation of state (EOS) in fractions of a single bunch train at very high pressures.

Similar to this we have been exploring the possibility of conducting dynamic compression experiments in the DAC to overcome the pressure threshold for the study of light elements such as molecular solids of H₂, He, methane etc. These compounds have the property to penetrate the diamond anvils and thus weaken their structure so that pressures above 3 Mbar at room or elevated temperatures are extremely difficult to reach and maintain. This is very evident in the recent experiments on hydrogen phase V (potentially metallic hydrogen) by Dalladay-Simpson et al. (2016) that reached pressure of close to 4 Mbar at room temperature and 3.5 Mbar at 460 K. However, these conditions could only be maintained for less than a day at room temperatures. Thus, the idea is to increase pressure rapidly at room conditions or high-temperature to conditions as high as 4 Mbar. In the past decade multiple groups have developed dynamically



driven DACs, for example in the pioneer work by the LLNL high pressure-group (Evans et al. 2007) that has, however, been limited to maximal compression rates of a couple of tens of GPa. This have been followed by newer developments of membrane driven DAC by the LANL high-pressure group reaching maximum pressure jumps in the 1 Mbar range and very recent efforts by synchrotron facilities such as HPCAT (Sector 16, Advanced Photon Source, APS) and the ECB (P02.2, PETRA III) to develop piezo driven DAC that can reach pressure in a controlled way and are getting closer to 1 Mbar (Sinogeikin et al. 2015; and Smith et al. 2015; Jenei et al. in preparation). Most of these studies have been performed in the lab using Raman spectroscopy or x-rays diffraction on heavy Z metals because collecting diffraction patterns at maximum compression rates of 34 TPa/sec (43 GPa/1.25 ms, Smith et al. 2015) at a 3rd generation synchrotron becomes more difficult when photon flux is too low to collect a full diffraction image or detectors are not fast enough. The full potential of these devices in terms of x-ray diffraction can only be explored at a XFEL that offers as much as 10^4 times more flux at high energies (20-25 keV), at fast repetition rates of up to 4.5 MHz, and the availability of detectors that can operate at the same frequency.

While both technical developments and their ultimate implementation will offer potential answers to important scientific question such as the location of B1- B2 transition in MgO or maybe even the location of the metallization of H₂, there are many more research projects (some that we cannot envision at the moment) at lower pressure and compression rates (e.g. Tomasino and Yoo 2013, Tomasino et al. 2014) that will provide answers because of the use of 4th generation light source.

In this “Conceptual Design Report” we like to introduce some of the obvious scientific challenges that may be addressed with such a new dynamic DAC setup proposed for the High-Energy Density (HED) instrument of the European XFEL (first experiment). In addition, and may be more importantly, we like to describe the technical implementation of such a dynamic DAC setup at the HED instrument and the technical difficulties encountered during the design phase as well as proposed solutions. One may add that the basic DAC setup will be funded as part of the Helmholtz International Beamline for Extreme Fields (HIBEF) approved in the summer of 2015. Thus, it is timely that we describe our vision and discuss it with the community before progressing to the next step of making detailed technical drawings and initiating construction. One of the added features that will be discussed in this CDR is the possibility of housing in the same small vacuum chamber (compatible to that under design for the Dynamic Compression Sector (DCS) at the (APS)) the setup for DACs as well as a small setup for a laser shock compression experiments optimized for x-ray diffraction crystallography experiments. This idea



has been recommended by the advisory committees of HIBEF and shall be approved on the basis of this final report by the HIBEF management board and HED.

2. Scientific Goal and Ideas using DACs at the European XFEL

Developing different DAC techniques for the European XFEL has been driven by two major scientific goals:

- a) Exploration of physical properties and stabilities of phases at the pressure / temperature condition of the interior of extrasolar planets (rocky as well as gaseous) currently not accessible with conventional static high-pressure conditions created in the DAC, and
- b) Exploration of compression rate dependence on physical properties and stability of phases in the strain rate regime above $10^{-1}/s$ to $10^4/s$ that can currently not be accessed at 3rd generation light sources, nor with shock compression at 4th generation sources.

There are new scientific areas developing as the community evaluates the technical possibilities of the European XFEL in conjunction with a dedicated DAC setup, like ultra-fast physical chemistry or WDM in the DAC. During the DAC CDR workshop at the end of January 2016 the DAC community suggested a series of new subject areas that we are adding here to the CDR:

- c) Exploring stellar interiors and fusion under WDM conditions in the isochoric heated DAC
- d) Thermal properties (thermal diffusivity) of mineral and melts at earth and other planetary core conditions via spectroscopy and x-ray diffraction
- e) Study early stages of melting as well as crystallization/phase separation processes at dynamic conditions through phase contrast imaging (PCI) and diffraction in normal and radial geometry in the DAC

Below we want to outline briefly the scientific cases for the subjects listed under a) and b) as well as attempted to sketch the relative new areas proposed under c) through e). The science covered under a) is subject of a Forschergruppe proposal that has been submitted to the DFG for their consideration. If this project is funded corresponding experiments will be performed using DACs at the European XFEL upon start of operation in 2018.

2.1. Study of phase properties and EOS at pressures and temperatures of the interior of extra-terrestrial planets

There are two experimental approaches, compared to existing static techniques, that one may achieve higher-pressure and -temperatures in the DAC, in order to explore physical properties in extrasolar planets under quasi static conditions: the double stage DAC (dsDAC, Dubrovinsky et al. 2012, 2015) and dynamical DAC (dDAC, Evans et al. 2007) technique. While the dsDAC (or variation of that) may be used for the exploration of metallic, rocky and gaseous constituents at pressure and temperature conditions of extrasolar planets' interiors, the use of the dDAC is envisioned predominantly for the study of light very mobile compounds up to 4 Mbar. Here the specific idea is that one may prevent the contamination/diffusion of light components into the diamond and thus extend its stability by increasing the pressure rather quickly. Given that we are interested in the exploration of super earth like planets and gas giants the following material systems seem to be most significant:

Rocky Planets

- Bridgmanite ($(\text{MgFe})\text{SiO}_3$)

Bridgmanite, ferromagnesian aluminosilicate perovskite ($(\text{Mg,Fe})(\text{Si,Al})\text{O}_3$), is the major constituent of the Earth's lower mantle and certainly also present in the interior of extrasolar planets. Its physical properties and crystal chemistry have been extensively studied using laser-heated diamond anvil cells (LH-DACs) that are routinely used to simulate conditions at the bottom of the lower mantle (130 GPa, >2500 K). Major discovery was the structural phase transition of bridgmanite into the CaIrO_3 -structure phase, called post-perovskite (PPV) (Murakami et al., 2004), which may be responsible for numerous anomalies observed by geophysicists in the D'' layer (Hirose et al. 2009).

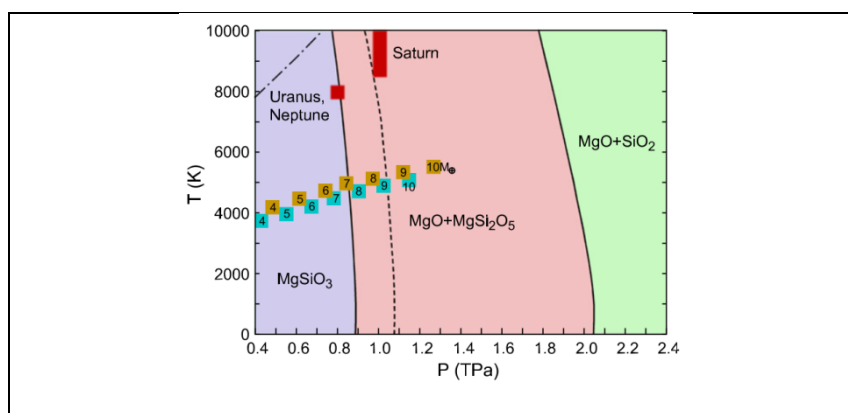


Figure 1: Phase diagram of MgSiO_3 post-perovskite according to first principles calculations up to 2.1 TPa and 10,000 K (Umemoto et al. 2011). P-T conditions of the two-stage dissociation of PPV are compared to the interiors of Uranus, Neptune and Saturn (in red) and to exoplanets with mass up to 10 times the mass of Earth (brown and cyan squares).



After this discovery new challenges have emerged, such as the question of what is the stability region of PPV and whether there exist further phase transitions at even higher pressures and temperatures. This extended phase diagram becomes of particular interest in the context of Earth-like exoplanets, with masses of up to 10 times that of the Earth (super-Earths) that are continuously being discovered. Experimental works on structural analogues of bridgmanite (for example, on FeTiO_3 ; Wu et al., 2009) indicate that silicate perovskite may decompose into ferropericlase and a complex $(\text{Mg,Fe})(\text{Si,Al})_2\text{O}_5$ compound. The fate of MgSiO_3 post-perovskite has been addressed to TPa pressures only by theoretical computations (Umemoto et al. 2011). Several dissociation stages were proposed at up to 2 TPa pressures (Fig. 1), which would have interesting consequences for giant planets in the Solar System, heavy super-Earths, and larger exoplanets. Saturn's, Uranus' and Neptune's cores are expected to be comprised of MgO and MgSi_2O_5 , whereas in Jupiter, MgSi_2O_5 should already be dissociated into MgO and SiO_2 . Stability of the PPV phase is predicted to extend to up to 900 GPa. In order to confirm these predictions we urgently need experimental data on the stability of bridgmanite.

- **(Mg, Fe)O**

Magnesium oxide (MgO) is representative of the rocky mantles in terrestrial planets such as Earth and super-Earths but also cores of Jupiter and other giant planets. This simple ionic oxide is stable to at least 300 GPa in the B1 (NaCl-type) structure [Oganov et al. 2003]. Due to the high symmetry of the structure and a lack of phase transitions, MgO is also widely used as a pressure calibration standard.

A new phase of MgO, B2 (CsCl-type), has been predicted by theoretical calculations at pressures exceeding 510 GPa [Oganov et al. 2003]. The Clapeyron slope of the phase transition is unusually steep (16×10^{-3} GPa/K), i.e. temperature has relatively small effect on the transition pressure. MgO is a wide-gap ionic insulator, which is predicted to be extremely difficult to turn into a metal – it requires pressures above 20 TPa.

The phase transition determined from decaying shock experiments (McWilliams et al., 2012) and ramp compression experiments (Coppari et al. 2013) is situated higher than the lines drawn by theoretical simulations (Cebulla and Redmer, 2014). However, the structural information evidences are only based on the appearance of a single extra diffraction peak.

Reaching the P-T conditions of this transition by means of static compression would represent a milestone in the technique and contribute to the accuracy of the phase diagram of MgO to better understand the interior of rocky extra-terrestrial planets.

- **Fe and Fe alloy**

Iron is a major constituent of Earth's core and thus its phase diagram up to 360 GPa has been extensively studied for more than two decades. However, the phase relations in Fe and Fe-Ni-light alloys above 2 Mbar and high temperatures have been questioned by many investigators using static compression techniques, shock waves and theory. Furthermore, the phase stability of Fe and Fe alloys is unknown at conditions that are expected in the cores of super-Earths, i.e. up to 2 TPa and 10,000 K.

Pure iron is stable in a hexagonal crystal lattice over a large P-T region – conditions close to Earth's inner core. However, molecular dynamics (Belonoshko et al. 2003) and ab-initio calculations (Luo et al. 2010) predict that pure iron adopts a body-centered cubic structure at high temperatures. These predictions have not yet been experimentally confirmed (Tateno et al. 2010, Ping et al. 2013).

Light element impurities in Fe-Ni cores would alter the phase relations compared to pure Fe. For example, bcc structure of Fe has been found by theory to become more stable by impurities such as Sulphur and Silicon under inner core conditions (Vocadlo et al. 2003).

- Melting curve of iron at high P-T provides key information to anchor the temperature at the inner-outer core boundary. However, the melting point at 330 GPa is veiled in controversies. The first experiments based on visual observation of melting (Boehler 1993) yielded temperatures extrapolated to the inner core significantly lower than those measured by the shock waves.
- To resolve these problems, experimental studies must reach these extreme conditions more routinely.

Gas Giants

Crucial to our understanding of Neptune-like exoplanets, and indeed to our understanding of the giant gaseous planets within our own Solar System, are accurate knowledge of the phase diagram, equation of state, phase transition kinetics, and the melting behavior of low-Z molecular systems planetary ices (Guillot et al. 1999), He and H₂ (McMahon et al. 2012).

- **Planetary ices (e.g. methane (CH₄))**

It is assumed that CH₄ accounts for 10-15% of the mass of Neptune. However, at pressures in excess of 20 GPa, the phase diagram remains poorly understood. Under increasing pressure, methane adopts a number of polymorphs of unknown structure (Bini and Pratesi, 1997).



Experimental studies indicated that methane dissociates to form hydrocarbons and carbon (Benedetti et al. 1999). This chemical breakdown of CH_4 inside Neptune and Uranus would allow the heavier carbon to sink and transform into diamond under the pressure and temperature conditions within the planetary interior. This dissociation is expected to have a significant effect on the internal evolution and energetics of these planets, but the dissociation curve is uncertain due to conflicting experimental results. It has been reported that methane undergoes a decomposition between 10-50 GPa at temperatures of 2000-3000 K (Benedetti et al. 1999), yet at room temperature no dissociation has been observed up to 200 GPa (Sun et al., 2009). Moreover, shock compression studies have observed no signal of decomposition up to 26 GPa and 3200 K (Nellis et al. 2001). Studies of this, and similar chemical/physical processes and their phase transformation kinetics, will provide unique insights into internal dynamics of planets, and aid in resolving the discrepancy between laser-heated static diamond cell experiments and shock compression studies.

- **He & H_2 and their mixtures**

Gas giants such as Uranus and Neptune are thought to contain high portions of planetary ices (see above) as well as mixtures of He and H_2 based on atmospheric composition and mean density of the planets (Fig. 2A). Models predict H_2 and He to be abundant in the outer envelopes and may be to a small extent in the interior of the planets (Nettelmann et al. 2013). Mixtures of H_2 and He and their demixing are predicted to occur in Saturn (e.g. Morales et al. 2009, 2013, Lorenzen et al. 2009, 2011, McMahon et al. 2012). In order to better predict the behavior of these mixtures in the interior of planets and constrain the models the community needs phase stability and EOS data on the individual compounds and their mixtures up to 1 TPa and 10,000 K. However, the stability fields of H_2 and He to such pressures and temperatures are not known as of today. Experimental data on the stability of He melting in the laser heated DAC are available up to 80 GPa (Santamaria-Perez et al. 2010, McMahon et al. 2012) while phase stability and EOS data are available up to 58 GPa (Loubeyre et al. 1993). Static high pressure data on H_2 phase stability data are now available up to ca. 350 GPa and 450 K (Fig. 2B, Dalladay-Simpson et al. 2016) based on Raman experiments in the resistive heated DAC.

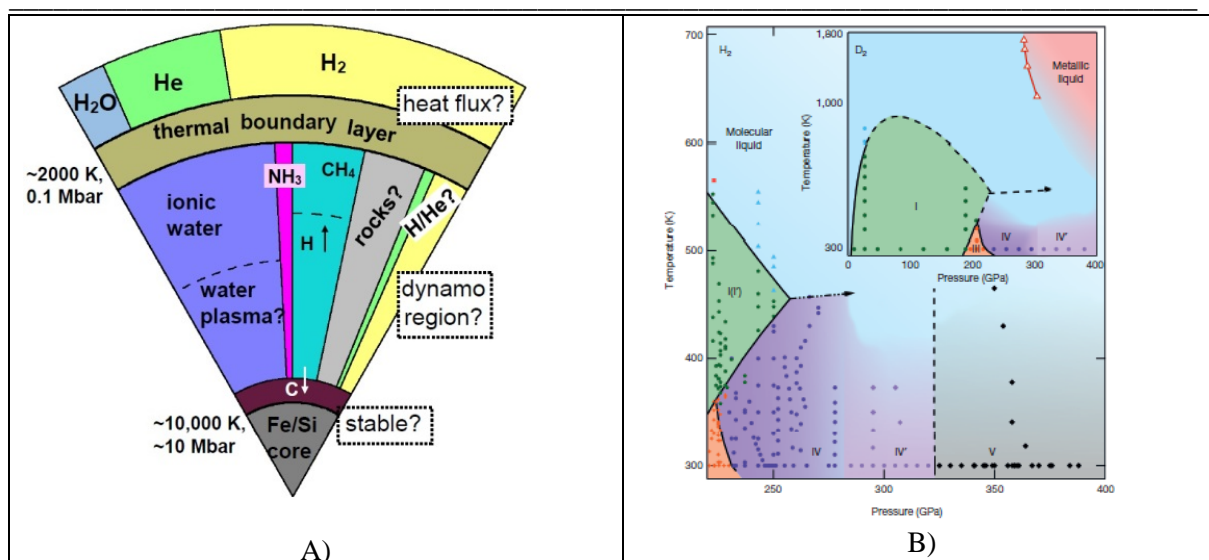


Figure 2: A) Possible internal structure of an Ice Giant Planet like Uranus (courtesy of N. Nettelmann). Colors indicate different materials as labeled. The outer, H/He-rich envelope may be separated from the ice-rich interior by a thermal, stable boundary layer. Methane in the deep interior may dissociate and form a stabilizing carbon layer. B) Phase diagram of H₂ from Dalladay-Simpson et al. (2016).

Hence, data on melting of He above 80 GPa are needed as well as solid phase stability and EOS data above 58 GPa. X-ray diffraction data on H₂ to constrain the EOS and verify Raman measurements are lacking all together. Experimental phase diagram data of mixtures of He and H₂ were given for room temperature up to about 80 kbar (Schouten et al. 1985, Loubeyre et al. 1987) and might be difficult to attain even with the flux available at 4th generation light sources because of the similarity of the two compounds. However, they would be highly valuable to confirm interior models and evolution scenarios for gas giant planets (see Püstow et al. 2016).

2.2. Compression rate dependence of physical properties

In the last decades there have been more and more evidence indicating the presence of compression rate dependence on the location of phase transitions and the morphology of the phase diagrams. Many of these observations originate from lower compression rate experiments in the membrane or piezo driven DAC and illustrate the significance of path dependence of phase diagrams (e.g. Chen and Yoo 2012, Chen and Yoo 2011, Tomasino et al 2013, Tomasino et al. 2014) and presence of metastable compounds that cannot form under static pressure conditions. While most of these experiments are done in lab environments using either fast micro Raman or micro-photography, recent advances at 3rd generation light sources enable fast compression experiments using x-ray diffraction (Liermann et al. 2015 and section 3.3.). Initial experiments indicate that rate and thus path dependencies are observable (e.g. on quartz polymorphs Carl et al. submitted and Bi polymorphs Jenei in preparation, Chen et al. 2014a, Chen et al. 2014b) but



full exploration of these dependencies is still limited to repetition rates in the kHz range. Recent advances in dynamic DAC design enable now compression rates of up to 32 TPa/s (Smith et al. 2015) that translates into strain rates in the 10^1 s^{-1} . Thus, further exploration of these path dependencies at higher compression and strain rates are significantly dependent on improved flux and higher repetition rates of the source and detectors, both of which will be offered by the HED instrument of the European XFEL. Furthermore, compression experiments at even faster compression rates using shock lasers e.g. on systems such as Bi indicate changes in the phase diagram all together (McMahon et al. personal communications) demonstrating the complexity of the path dependent compression. Hence, a full understanding of these pathway dependencies really requires further increase of strain rates as of today of 10^1 s^{-1} accessible with the dDAC (Smith et al. 2015) to 10^7 s^{-1} commonly reached during laser shock compression. One may also explore during these experiments material behavior far from mechanical equilibrium, to be able to detect previously unknown states of matter under extreme elastic compression (Crowhurst et al. 2011, Whitle et al. 2011) sub-100 ps martensitic phase transitions (Crowhurst et al. 2014) and strain rate dependent shock induced chemistry (Armstrong et al. 2013, Gilman 1995, Armstrong et al. 2010). In this variation of the classic dynamic driven DAC experiment the pre-compressed DAC samples will be exposed to a ultrafast laser compression (<200 ps) (Armstrong et al. 2010) and probed with XRD in the time domain of 10-100 of fs. Latter will address questions of relaxation times and mechanisms (e.g. through intermediate states Mundy et al 2008) of phase transitions, and the results obtained on such short time scale can be directly compared to those of theoretical MD simulations. Results of such experiments might also provide access to metastable phases.

As evident from the slowly emerging publication in this field of compression rate dependent research, the field is still in its infancy and is mostly concentrated on the study of model systems that are very well understood under static high-pressure and simultaneous high-temperatures. Thus, the kinetics of phase transformations under conditions of high strain rates (e.g. faster than relaxation to thermal equilibrium) and large deviatoric stresses is of great importance for understanding of planetary impact phenomena such as meteorite and asteroid impact on the earth and other extra-terrestrial planets as well as collision studies between different planetary objects.

2.3. Exploring stellar interiors and fusion under WDM conditions in the isochoric heated DAC

The characterization of matter at high densities (similar to the solid state, and larger), intermediate temperatures (a thousand to a million degrees K), and fast (microsecond-



nanosecond) to ultrafast (picosecond to femtosecond) timescales, is central to our understanding of planetary and stellar interiors, fusion energy technologies, and the fundamental interactions in matter at extreme conditions. Many relevant and poorly-understood phenomena at these ‘warm dense matter’ conditions are found only at elevated densities, such as fluid-fluid phase transitions, phase separation of noble gases, and metallization in molecular materials (Lorenzen et al., 2009). Knowledge of how increasing density influences fundamental interactions including rates of bond dissociation and electron-ion thermal equilibration are also needed (Zastrau et al., 2014). Laser-compression platforms at FEL beamlines are not well-suited for the study of many molecular materials at these high densities, owing to their high compressibility. The manipulation of density by pre-compression in a DAC prior to excitation and probing offers a potential alternative tool to explore relevant warm-dense states of such substances and determine onset of molecular dissociation and liquid-liquid phase transition by x-ray scattering (Weck PRB 2007; Zastrau et al., 2014 ;Lorenzen PRL 2009); the study of phase separation of helium-hydrogen mixtures using, e.g. phase contrast imaging; and the measurement of electron-ion equilibration at many-fold compressions above solid density via femtosecond x-ray pump-probe heating and structural observations (Zastrau et al., 2014, White et al. 2014). Compared to traditional isochoric heating experiments, pre-compression and tamping by thick anvils can enable exploration of novel regimes of density, temperature, and timescale in warm dense matter.

2.4. Thermal properties (thermal diffusivity) of mineral and melts at earth and other planetary core conditions

The heat transport through minerals and melts at extreme pressures and temperatures is of central importance for understanding the dynamo, magnetic field and consequently the thermal history as well as dynamics of planets (e.g. Konôpková et al., 2016). Of particular interest is the determination of thermal conductivity of Fe alloys in the molten state as well as mantle minerals at core-mantle boundary (CMB) pressures and temperature conditions. By combining pulsed laser heating and XRD capabilities of the European XFEL at the HED instrument, we will be able to measure thermal conductivity of deep planetary materials including those in the liquid state. The experiment will require single shot time domain measurements of thermal expansion of metallic transducers deposited on the sides of the sample pre-compressed in the DAC and pulse laser heating (Konôpková et al., 2016; McWilliams et al., 2015; Beck et al., 2017).

2.5. Study of early stage of melting and crystallization via phase contrast imaging (PCI) and diffraction in normal and radial geometry



Melting and crystallization phenomena are central for understanding the material behavior under extreme P - T conditions, as reaching the molten state allows direct probes of the strength of interatomic interactions such as the shear modulus. Although there exist extensive literature results on the melting behaviors of many materials, significant discrepancies in the reported melting curves of refractory metals remain (e.g. Dewaele et al. 2010). In the proposed experiments single pulsed laser heating (100 ns to few microseconds) will be combined with time-domain XRD diffraction that will be used to detect Bragg reflections of solid and diffuse rings of liquid during melting and crystallization. Part of these studies will be also a combination of PCI and x-ray diffraction to assess the precise location of the onset of melting/crystallization, e.g. at the edge of the gasket or the interface of the diamonds. Determination of the onset of melting at the diamond - sample interface in the sample chamber will be very important since it has direct implication for the activation energy of melting. These new area of experiments will help to resolve controversies about melting curves of refractory metals to >100 GPa range.

In summary, the above described experimental cases studies give an initial overview of what scientific questions we hope to address with a dedicated DAC setup at the HED instrument of the European XFEL. Below we will review the status of the experimental techniques to answer the above scientific questions, particularly keeping in mind the limits that one encounters when conducting these experiments at 3rd generation sources.

3. DAC techniques

We will shortly summarize the technical status of the different DAC techniques and the future development anticipated towards their implementation at the HED instrument of the European XFEL.

3.1. Dynamic DAC

There are several ways to dynamically compress samples in the DAC. The simplest version uses a membrane (double manifold) that is very quickly inflated as demonstrated by recent studies of Velisavljevic et al. 2014 or Konôpková et al. 2015. With this technique the researchers have reached pressures of as close as 1.3 Mbar with compression rates of 400-500 GPa/s (Velisavljevic et al. 2014, Smith et al. 2015). However, in many x-ray diffraction studies these high compression rates have not been applied because either the speed of the detector or the flux available at 3rd generation light sources was insufficient. Thus, many studies have been performed in laboratory environments using analytical techniques such as resistance measurements (Velisavljevic et al. 2014). Furthermore, the disadvantage of using a membrane driven DAC is the very little control on the compression curve, i.e. the way that the pressure increases is dictated by the response of the membrane (or diaphragm) and the gasket/sample assembly (Smith et al. 2015, Fig 2; Konôpková et al. 2015 see Fig. 1 & 3 within).

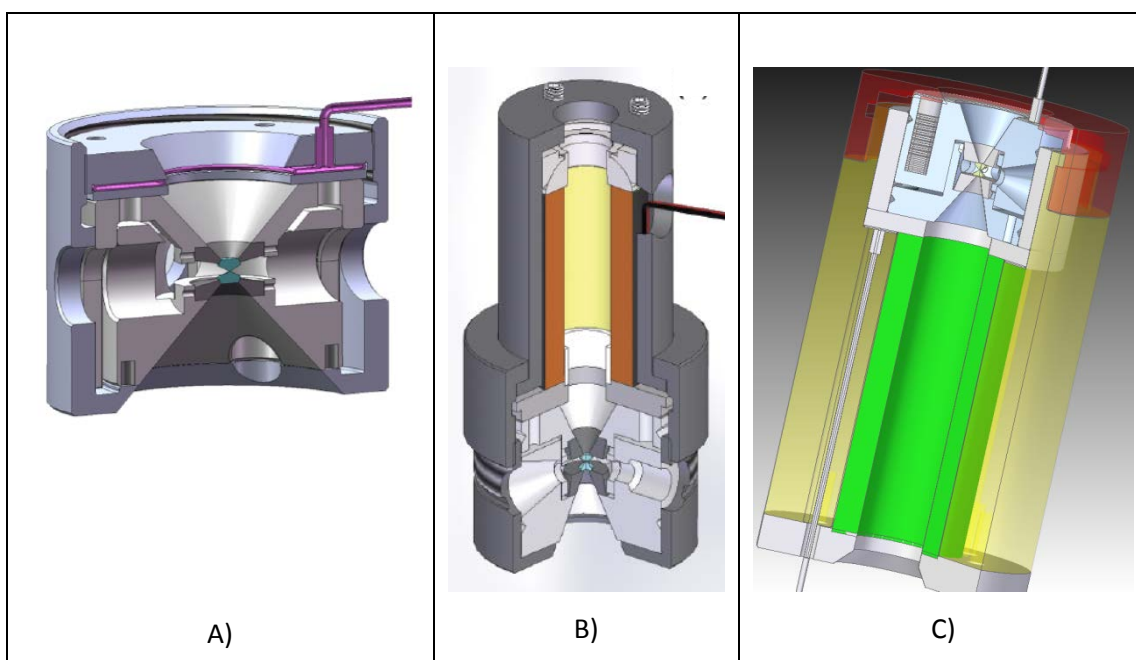


Figure 3: 3D representations of membrane driven and piezo driven DACs. A) and B) are from Sinogeikin et al. 2015 and C) from Konôpková et al. personal communications.

More control on the compression curve can be attained when using electromechanical actuators (piezo) as originally developed by the LLNL high pressure group (Evans et al. 2007). This so called dynamic DAC offers compression as high as the membrane DAC (400-500 GPa) but much better control on the compression curve since the movement of the actuators can be controlled by a frequency generator (max 500 Hz at the moment). As in the case of the membrane DAC maximum attainable compression rates have not been applied to x-ray diffraction experiment because of slow detectors and insufficient flux (e.g. Chen et al. 2014a, b). Raman and especially high speed photography have been used to make use of maximum compression rates (Tomasino and Yoo 2013, Tomasino et al. 2014). Very recently the speed and sensitivity of x-ray recording detectors has increased significantly (Silicon Pilatus 1 M, 500 Hz max frame rate, Silicon Eiger 1M, 3 kHz max frame rate, GaAs LAMBDA 2 M, 2 kHz max frame rate) so that faster x-ray diffraction experiments have become possible and hence the dynamic DAC was further developed to achieve even faster compression rates in the TPa regime (34 TPa/s Smith et al. 2015, Sinogeikin et al. 2015, 7 TPa/s Jenei et al. in preparation). These new developments are still at the beginning and one might be able to increase compression rates further by varying the size of the culets, gasket materials, etc. Currently, using 0.15 mm culets culminated in a pressure increase of 43 GPa (Smith et al. 2015) and 40 GPa (Konôpková, personal communication). In the coming years further developments of the dynamic DAC technique is necessary in order to achieve pressure differentials in the multi Mbar regime to conduct experiments proposed in the scientific section (2.1 and 2.2). However, it is already clear that experiments with above pressure differentials and high compression rates, previously only possible with high speed photography, should now be possible using x-ray diffraction because of the increased flux, the time structure of the European XFEL and speed of the new detectors, all of which is proposed for the DAC setup at the HED instrument (see section 3.3). In addition we are planning to equip the piezo driven DACs with resistive heaters as already shown by Chen et al. 2014 and combine it with laser heating or isochoric heating.

3.2. Double Stage DAC

For decades the pressure limit for static DAC experiments has been about 4 Mbar and 4000-5000 K (e.g. Tanten et al. 2010). In 2012 this barrier was surpassed by the development of the double stage DAC (dsDAC) technique (Dubrovinsky et al. 2012) reaching pressure of 640 GPa on gold and rhenium. Consequently, there have been several publications using similar approaches (Lobanov et al. 2015, Sakai et al. 2015) with a most recent studies report pressures of 775 GPa on osmium (Dubrovinsky et al., 2015) and over 1

TPa on gold (Dubrovinsky et al., 2016) at room temperatures and it seems that the maximum pressure is not in sight as of today. Further work on implementing secondary gaskets in order to create a chamber with more hydrostatic conditions are also on the way. These improvements will be essential to create very high pressures in liquids and gases, a further extension of the technique. While these studies are conducted at the moment exclusively at room temperatures and on heavy Z compounds, they point towards a new chapter in high-pressure research aiming at exploration of pressure and temperature conditions in extra-terrestrial planets and new physical properties (Dubrovinsky et al. 2015).

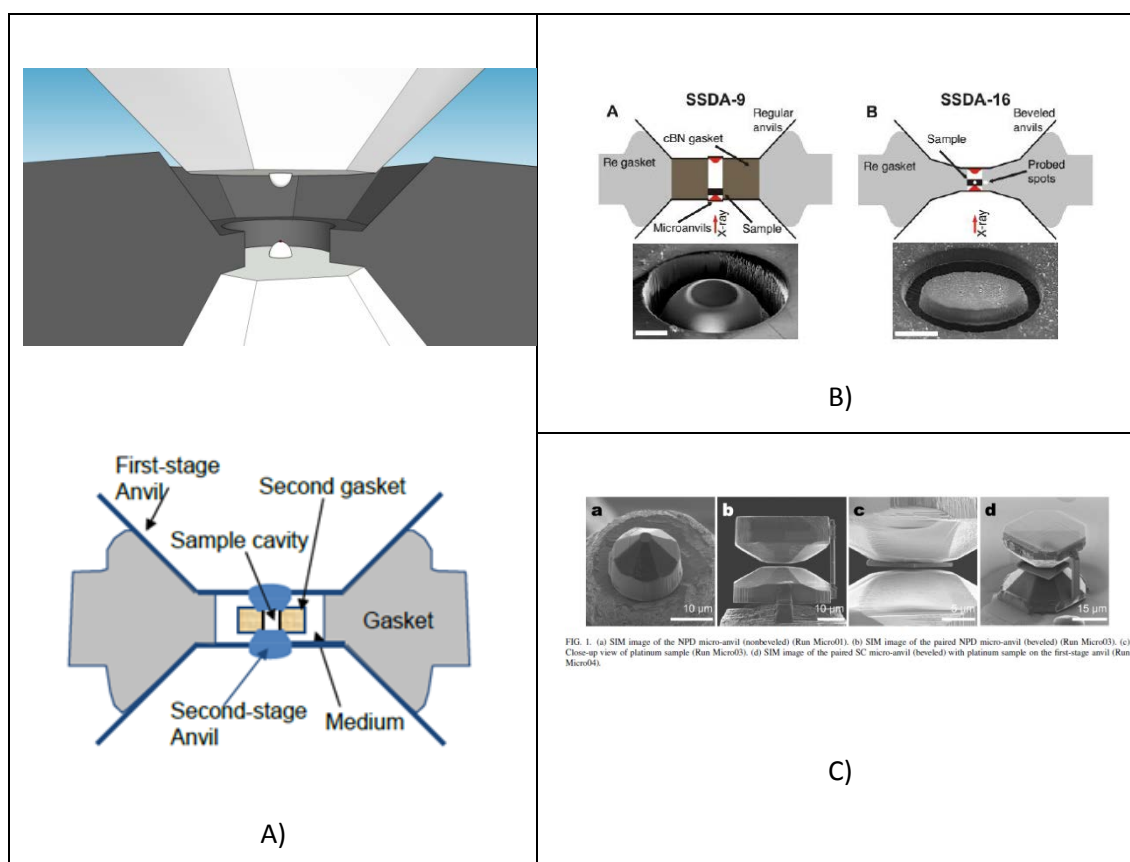


Figure 4: A) Schematics of the dsDAC setup by Dubrovinsky et al. (2012, 2015) B) Schematics and SEM images from Lobanov et al. 2015 and C) SEM images from Sakai et al. 2015.

Laser heating experiments with infrared lasers in the dsDAC have been attempted but provided insufficient results because the second stage anvils lost very quickly their strength and as consequence the pressure on the sample dropped (Dubrovinsky, personal communication). The reason why the second stage anvils are so susceptible to increase in temperature is not yet clear. However, this pressure drop can be bypassed if diffraction patterns are collected more rapidly, i.e. on ns to μ s time scale. This is currently not possible at any of the 3rd generation light sources (even at diffraction limited storage rings proposed



for the future) mostly because of insufficient flux. The only alternative is to conduct dsDAC experiments at the European XFEL and specifically the HED instrument.

3.3. Do we need the European XFEL and how would a dDAC/dsDAC experiment at the HED instrument be conceptually setup?

One may wonder if either the dynamically driven DAC experiments or the dsDAC experiments could also be performed at the existing 3rd generation light sources. In the last years, various high-pressure beamlines at 3rd generation light sources have tried to improve their performance (beam size, flux and detector speed) to optimally support experiments of both DAC techniques. Here we discuss the limitation one will encounter at 3rd generation sources by presenting some recent experimental efforts at the Extreme Conditions Beamline (ECB) at PETRA III in Hamburg, Germany. At the same time we like to describe the type of experiments one can expect at the HED of the European XFEL.

Dynamically driven DACs can reach compression rates of up to 34 TPa/s over a pressure range of about 40 GPa. While this is certainly not the limit for this technique we are unable to get more than a few diffraction patterns with the existing flux and detector speed. At the ECB we conducted recently diffraction experiments on the fast compression of Bi and reached compression rates of 1 TPa/s (Jenei et al. in preparation). Data were collected at 25.6 keV with a Compound Refractive Lens (CRL) focused beam of $8 \times 3 \mu\text{m}^2$ on a new GaAs LAMBDA detector (X-Spectrum GmbH with 95 % quantum efficiency at 25 keV). At the given beam parameters that provides an approximate flux of 8×10^{11} ph/sec in the focus and with a 20 μm thick sample of a heavy Z-compound such as Bi, we were able to collect good diffraction data at a frame rate of 2 kHz (0.5 ms). From all available hybrid pixel detectors the GaAs-LAMBDA detector is at the moment the one with the fastest read out speed for this particular energy. Currently, this seems to be the limiting factor for this type of experiments. While further detector developments might offer higher frame rates in the future, the sensitivity of the detectors will not be better because the GaAs chip offers already a quantum efficiency better than 95 % at 25 keV. From our recent Bi compression experiments we believe that at 25.6 keV (lowest energy and highest flux for this beamline, see Liermann et al. 2015) we have maximized the time resolution and reducing collecting time will result in poor quality diffraction patterns. There are a few more things one can do to increase the time resolution, e.g. one might use pink beam (now available at the ECB) offering flux of the full undulator harmonic. This increases the flux by a factor of about 30 at the ECB, at the cost of poorer instrumental resolution and the presence of lower and higher undulator harmonics (making the evaluation of the data more complicated). However, this

will get us at most to the 10th of micro seconds on heavy Z compounds. For the dynamically driven DAC experiment proposed earlier we want to collect good diffraction images at even higher frame rates, at shorter exposure time (to snap just one state) and most importantly on low Z compounds like H₂, He, methane, etc. As it has been shown by several recent studies at the Matter of Extreme Conditions (MEC) station at the LCLS it is possible to collect diffraction image in 10th of fs. For example, Gorman et al. (2015) collected on 0.02 mm thick Bi foil in 80 fs a decent diffraction image and at the same exposure time a scattering signal from shocked melted Bi. This highlights the potential of conducting diffraction experiments at the HED instrument of the European XFEL. Together with the fact that the European XFEL will be able to operate at 20 – 25 keV on its principle harmonic, offering 100 fs long pulses at repetition rates of 4.5 MHz and flux of 10¹² ph/pulse, it will be the ultimate place to conduct fast compression experiments in the dynamically driven DAC. We will show in section 4.3. that we in fact can expect to collect diffraction pattern in 100 fs on a 0.02 mm thick iron foil in a DAC. In Fig. 5 we depict one possible scenario for conducting a dDAC experiment. Here we want to compress a sample to the highest possible pressure and collect diffraction patterns over one bunch train of 600 μs (see Fig. 5) to get a complete EOS before the diamonds break. The AGIPD detector will only be able to collect a total of 350 images out of the 2700 x-ray pulses but the read-out frequency can be varied from 583 kHz up to 4.5 MHz.

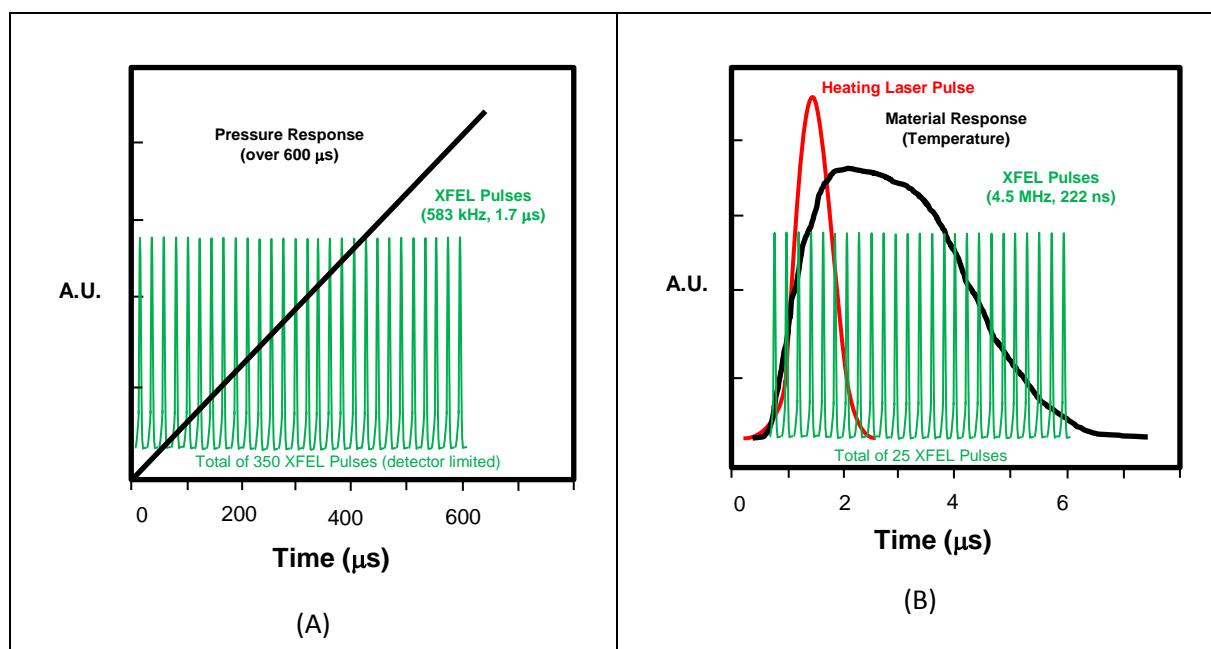


Figure 5: Schematic view of the expected timing for dDAC (A) and dsDAC (B) experiments at the DAC setup for at the HED instrument of the European XFEL. In the case of the dDAC experiment the limiting factor will be the fact that the AGIPD detector will only be able to collect 350 images in burst mode (more when pulse duration and collection times are longer).



When conducting dsDAC experiments at 3rd generation light sources it is most important to collect diffraction images with a very small beam with as much flux as possible in order to reduce the pressure gradients that this technique inherently produces. At the ECB we have been able to create a beam of 2.5 μm with a tail of 10 μm and flux of 2×10^{11} at 25.6 and 2×10^{10} per second at 42.7 keV (Liermann et al. 2015). The flux is lower in comparison to the dDAC experiments because we are cutting off significant portions of the tail with a pinhole. Smaller beams would be desirable, but at the cost of a significant flux reduction (more CRL or smaller KB system). For room temperature experiments a smaller beam with reduced flux will be sufficient because collection times would just increase. If one would try to collect diffraction images of a heated sample at the ECB with pink beam and the LAMBDA detector one might be able to collect diffraction images in 10 – 50 μs and thus the heating pulse could be as short as 10 μs . However, using a much smaller beam would decrease flux and scattering, resulting in poor or no diffraction image. This issue becomes even more pronounced if you want to study lower Z compounds like MgO or even molecular solids. So particular for the short duration experiments at high temperatures we will need the 100 fs pulses of the European XFEL with a repetition rate of 4.5 MHz. Fig. 5 (B) illustrates what a pulsed laser heating experiment at the HED instrument could look like. Here we reduced the laser pulse FWHM to 1 μs resulting in the material response of 8-10 μs . Any short duration might result in non-equilibrium conditions, which we like to avoid for EOS or phase diagram studies encountered in planetary materials but that might be interesting if you want to study non equilibrium processes. At a pulse train repetition rate of 4.5 MHz we would theoretically be able to place 25 x 100 fs long pulses and collect the same amount of diffraction images of the sample. This duration will be short enough to eliminate the significant drop of pressure on the second stage anvils. There are some constraints from the damage threshold of the diamonds due to deposition of the larger number of photons per pulse, but we will discuss this issue in section 5.

In summary, conducting dDAC and heated dsDAC experiments at the HED instrument of the European XFEL would allow us theoretically to collect diffraction images faster by a factor of 10^9 (from $\mu\text{s} \Rightarrow \text{fs}$) at an repetition rate increase of a factor of 10^3 (kHz \Rightarrow MHz) in comparison to the best of 3rd generation light sources. Finally, one should note that none of the experiments above are possible at other 4th generation sources but the European XFEL because a) the x-ray energy of these sources cannot provide energies of 20-25 keV essential to penetrate the diamond anvils effectively and reduce the absorption and damage in the

sample as well as access to reciprocal space, and b) because repetition rate of the other sources is limited to a maximum of 120 Hz (LCLS) and 60 Hz (SACLA) at the moment.

Table 1: Overview of the current limitation to conduct dynamic diffraction experiments at 3rd generation light sources (e.g. ECB) and expected limits at the HED of the European XFEL.

Experiment	Energy (keV)	Beam size (FWHM, μm^2)	Pulse Length	Flux	Max rep. rate	Max rep. rate
ECB			(μs)	(ph/s)		(kHz)
dDAC	25.6 (42.7)	3 x 8	50-100	8×10^{11}	n.a.	2
dsDAC	25.6 (42.7)	2.5 x 2.5	50-100	8×10^{11}	n.a.	2
HED			(fs)	(ph/s)	(MHz)	(MHz)
dDAC	20-25	2 x 2	50 – 100	10^{11}	4.5 ^{*,+}	4.5 ^{*,+}
dsDAC	20-25	1 x 1 (0.1 x 0.1)	50 – 100	10^{11}	4.5 [*]	4.5 [*]

* Within pulse train. + Limited to 350 images (77 μs) in the AGIPD detector burst mode.

4. X-ray Beam Requirements and Expected Scattering Power

As stated in the above section 3 it is essential to have varying foci available at the HED instrument of the European XFEL. Furthermore, it will be essential to reduce the damage threshold on the diamond when placing 100 fs photon pulses in the DACs (see section 5) which will have a huge effect on our capability to perform these experiments before the diamonds melt or sublimate. In addition it is very desirable for the dsDAC experiments to have nano focusing capabilities that will be provided by HIBEF consortium (Workpackage x-ray Instrumentation). The HED instrument can offer two interaction points (IA), one in the main chamber at 972.5 m (IA1) from the source and a second one 4.5 m downstream at 977 m from the source (IA2). Because of the implementation of a portable infrared laser heating setup that includes streak cameras for fast temperature measurements in the DAC and the necessary space requirement, it was proposed to locate the DAC setup at IA2. Below we describe the bunch structure of the European XFEL for completeness and the current focusing schemes foreseen of the HED instrument. Finally, we will present some calculations on what scattering power one can expect from a sample such as iron in the DAC.

4.1. Bunch Structure of the European XFEL

The peak brilliance as function of energy and bunch structure of the European XFEL is described in Fig. 6. The increased peak brilliance of the European XFEL originates from the fact that one 100 fs bunch has as many photons (2.2×10^{11} ph/pulse, see table 2) as the 1 s x-ray beam created at

3rd generation light sources. At the same time the bunch structure of the European XFEL is very different to that of a 3rd generation source that usually operates in a continuous bunch pattern mode, e.g. at PETRA III in the 40 bunch mode separation is 196 ns between pulses. At the European XFEL the bunches also are going to come in very short repetition, i.e. 222 ns apart, but only a maximum of 2700 in one 0.6 ms bunch train. In 1 second there will be 10 of this 0.6 ms bunch trains with a separation of 99.4 ms.

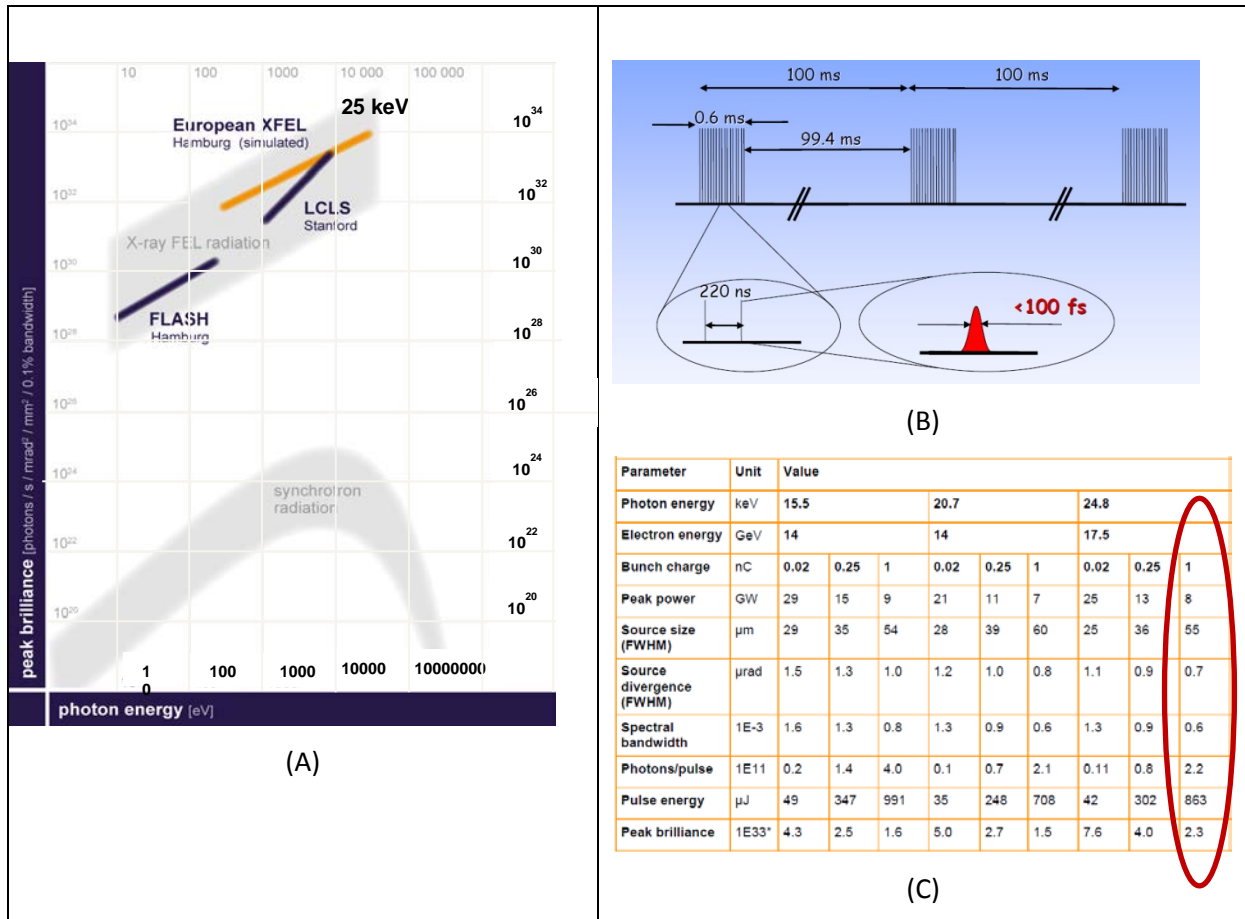


Figure 6: (A) Peak brilliance as function of photon energy of the European XFEL. (B) Bunch structure of the European XFEL with in train repetition rates of 4.5 MHz and bunch train repetition rate of 10 Hz. (C) Table 2 of photon beam parameters expected for the HED instrument that is located at SASE 2 (Self-Amplified Spontaneous Emission) reproduced from the TDR of the HED instrument Table 4-2. At 24.8 keV and bunch charge of 1 nC, each bunch has about 2.2 x 10¹¹ ph/pulse similar to what one would expect in 1 s at a 3rd generation light source.

4.2. CRL focusing (provided by HED)

Focusing at the HED instrument will be accomplished through Compound Refractive Lenses (CRLs). Fig. 7 (Figure 4-6 from HED TDR) shows the different focusing scenarios proposed for the HED instrument employing three different CRL package systems located at 229 m, 857 m and 962 m from the source. Table 3 (Table 4-4 from HED TDR) indicates further that a 1 x 1 μm² (FWHM) focus can be accomplished with focusing scenario (f) that uses an intermediate focus at 595.5 m created by CRL 1 and a final focus device at 962 m

from the source called CRL 3 (located within the HED optics hutch) resulting in a 92 % transmission of the incident beam.

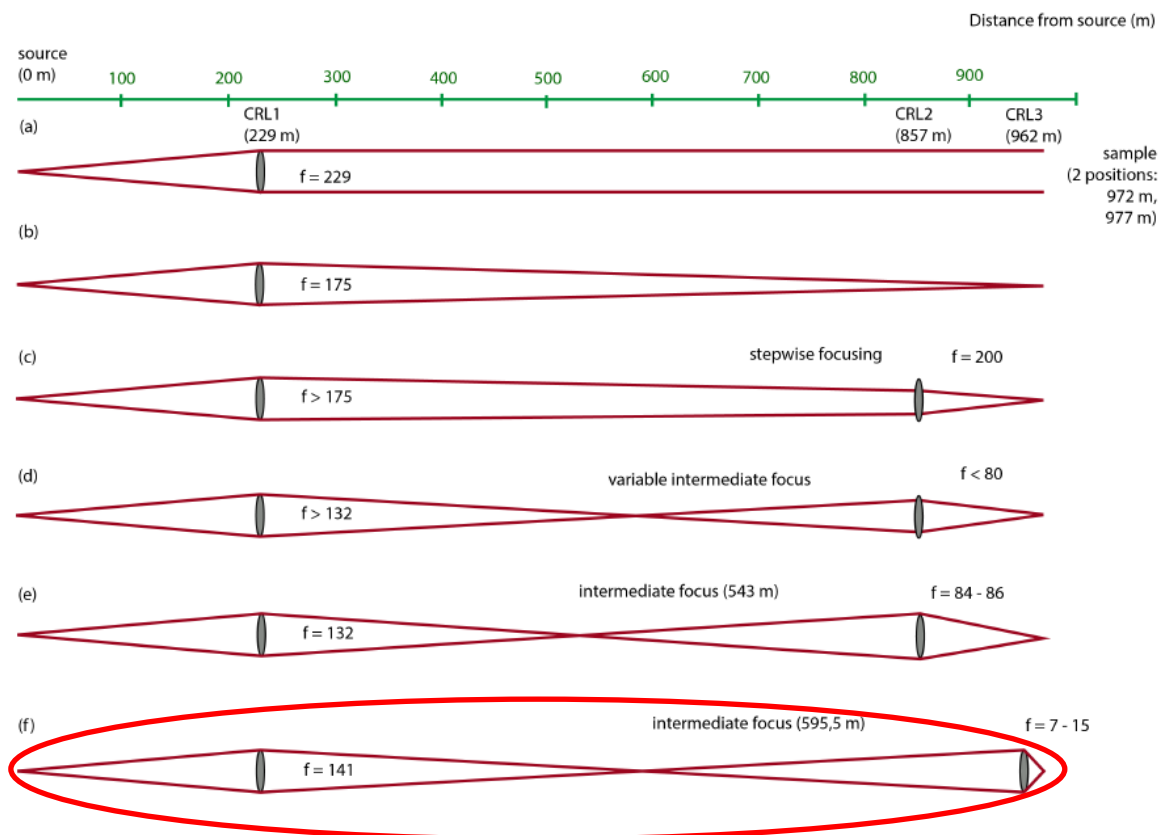


Figure 7: Different focusing schemes proposed for the European XFEL (reproduced from Fig. 4-6 of the TDR of the HED instrument at the European XFEL).

Focusing at IA1 (972 m from the source) and IA2 (DAC, 975 m from the source) with CRL3 to the micrometer range requires a significantly different focal length for the CRLs. However, the HED instrument will provide sufficient CRL lenses to achieve a focusing to the micrometer range at both positions, i.e. for IA1 in the energy range between 5-22 keV and for IA2 between 6-25 keV. Fig. 8 shows x-ray tracing simulations of the focus at IA2 (974 m from the source) indicating a focus of below $2 \times 2 \mu\text{m}^2$ (FWHM). Due to the diffraction limit of about $1 \mu\text{m}$ for the distance between CRL3 and IA1 and IA2 smaller spot sizes can only be achieved by moving a nano focusing lens system closer to the sample (see section 4.3).

Table 3: X-ray beam parameters for IA1 as function of energy and focusing scenario. For the DAC setup we will use scenario (f) at 25 keV

CRL geometry X-ray energy	Focal spot FWHM [μm]	Transmittance	Intensity [W/cm^2]
(f) 5 keV	2.6	0.55	$\sim 1\text{E}17$
15 keV	1.3	0.92	$2\text{E}17$
25 keV	1.1	0.93	$5\text{E}17$
(e) 5 keV	40	0.92	$1\text{E}14$
15 keV	26	0.99	$1\text{E}15$
25 keV	24	0.99	$1\text{E}15$
(b) 5 keV	260	0.97	$4\text{E}12$
15 keV	190	0.99	$2\text{E}13$
25 keV	160	0.99	$5\text{E}13$

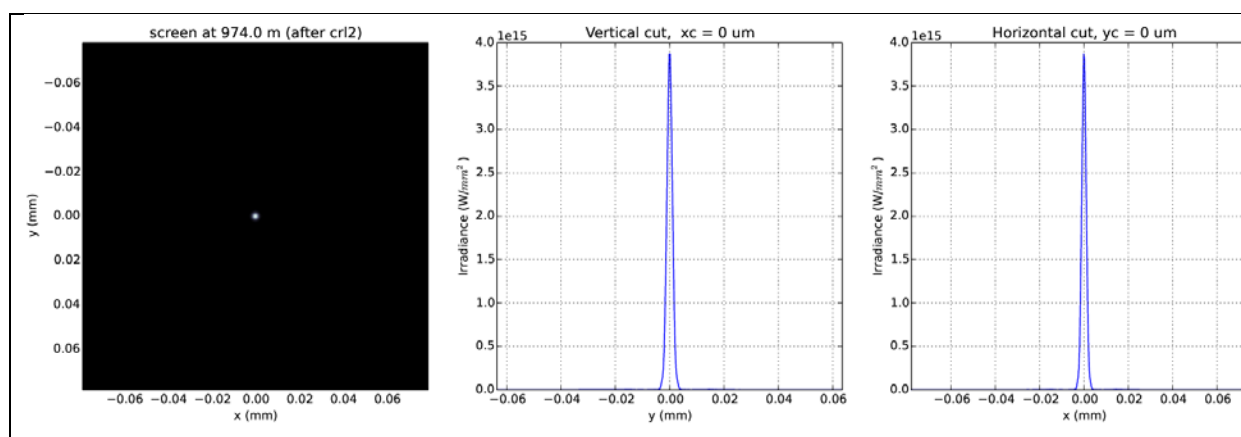


Figure 8: X-ray tracing information for the IA2 at 974 m from the source with focusing scenario f (Fig. 7) provided by K. Appel (European XFEL, personal communication). Focal size is below $2 \times 2 \mu\text{m}$ (FWHM) at this position. Larger foci can be achieved by combining different CRL packages.

4.3. Nano focusing (provided by Workpackage x-ray Instrumentation)

A nano-focus option will be of special interest for the dsDAC experiments since typical samples are small and show large pressure gradients within tiny areas of a sample. In order to be able to resolve these pressure gradients locally, we aim to implement a nano-focusing setup into the DAC-chamber. This setup is not part of the baseline instrumentation provided by the HED instrument, but will be contributed by the HIBEF consortium. The setup will be similar to the Phase-Contrast Imaging (PCI) setup built for the MEC station at the LCLS (Fig. 9) and will provide x-ray foci with a size of about 100 nm and below.

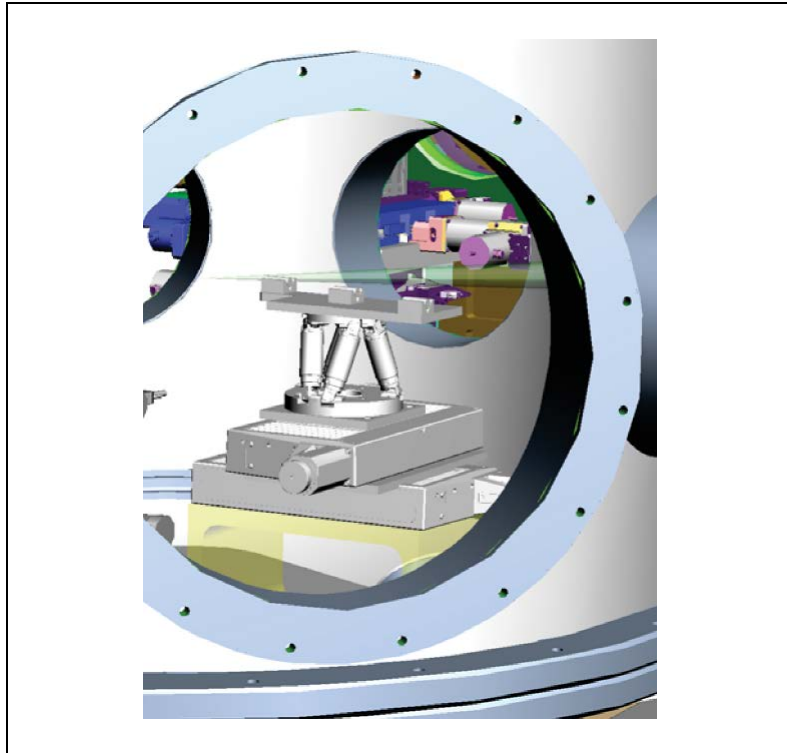


Figure 9: 3D representation of the nano focusing setup originally designed for PCI in the vacuum chamber for the DAC setup.

Table 4: Shown parameters include the focal length f , the number of lenses N , the numerical aperture NA , the diffraction-limited spot size D_t (FWHM), and the expected photon flux per pulse assuming an incoming photon intensity of 10^{12} photons/pulse/mm².

E [keV]	f [mm]	N	NA [mrad]	D_t [nm]	Flux [ph/pulse]
10	100	90	2.1	44	$1.6 \cdot 10^{10}$
	200	38	1.2	77	$2.9 \cdot 10^{10}$
	300	25	0.9	107	$3.7 \cdot 10^{10}$
25	250	228	0.9	41	$2.1 \cdot 10^{10}$
	350	142	0.7	54	$2.7 \cdot 10^{10}$
	450	106	0.6	67	$3.2 \cdot 10^{10}$

The nano-focusing setup will be located in the vacuum chamber for the DAC setup or in an additional chamber located upstream. Table 4 summarizes the anticipated focusing parameters at two typical x-ray energies E using state-of-the-art compound refractive x-ray lenses made of Beryllium (Be-CRLs) with a radius of $50 \mu\text{m}$ and aperture of $\sim 300 \mu\text{m}$ at 25 keV. Since a single refractive lens is typically not focusing strong enough, multiple of these lenses N have to be stacked behind each other to finally yield the desired focusing properties.

4.4. Scattering power

Estimation of the scattering power of the sample in the different DACs is essential to carefully plan the experiment, i.e. what incident beam flux is necessary to create enough scattered photons to be detected on the different detectors. We used the theory from Blome et al. 2005 to estimate the scattering power from iron with different sample thicknesses in the DAC. The details of the calculations are listed in Appendix A. In Table 5 we show that each pixel of a detector with a 0.2 mm pixel size that is exposed with the center of the (110) reflection of iron will receive about 10^4 to 10^5 photons per pulse assuming an incident flux of 10^{11} to 10^{12} , respectively.

Table 5: Calculations for N_p (photons per pixel) for (110) reflection of a 20 μm thick iron foil based on Blome et al. (2005). Details of the calculations are shown in Appendix A.

Scenario	N_0 (ph/pulse)	T	N_{eff} (ph/pulse)	A (μm^2)	V (μm^3)	$IF_{(110)}^2$	$\theta_{(110)}$ (degrees)	$N_{(110)}$	N_p
25 keV ($\Delta E/E 10^{-3} \text{ BW}$) _{vac}	10^{12}	0.640	6.4×10^{11}	1	20	1401.943	7.027	3×10^5	2×10^5
				4	80	1401.943	7.027	3×10^5	2×10^5
25 keV ($\Delta E/E 10^{-4} \text{ BW}$) _{vac}	10^{11}	0.640	6.4×10^{10}	4	80	1401.943	7.027	3×10^4	2×10^4

The Perkin Elmer (one of the detectors considered for these x-ray experiments) requires 80 ph/ (pulse, pixel) to be above the background to detect a diffraction signal. However, according to Blome et al. (2005) this will be not enough to get a good diffraction pattern with reasonable statistics. It may be pointed out that with an increase of the beam size the number of photons/area decreases and thus there is less potential to damage the diamonds and the sample, while the overall scattering power will stay almost constant. This fact will be important for considering the damage threshold on the diamond anvils and the sample. Thus, the deciding factor for the beam size is the spatial resolution that one wants to achieve within the dsDAC in order to estimate accurately pressures of the sample. A $1 \mu\text{m}^2$ beam (or less) will result in a very good pressure resolution but will at 10^{11} ph/pulse damage the diamond after one shot. However, at a minimum required scattering power N_p of 10^4 ph/(pulse, pixel), one can still lower the power of the incident beam by a factor of 10 and get good statistics while avoiding diamond damage. One may also note that when reducing the thickness of the sample from 20 μm to 2 μm thick iron foil the scattering power will scale linearly by a factor of 10. Consequently, at the highest pressure when the sample is only 2 μm thick or less scattering power will be 10^2 ph/(pulse, pixel) when the incident beam carries 10^{10} ph/pulse.

Another point to discuss is the question what the coherence of the beam would do to the diffraction image. This issue has been discussed and it was found that it will play only a

minor role because the 25 keV coherence is significantly reduced in comparison to 8 keV and diffraction experiments at the MEC station of the LCLS indicate that the diffraction experiments at 8 keV still yield decent diffraction images (Gorman et al., 2015).

5. Diamond Anvil Damage thresholds

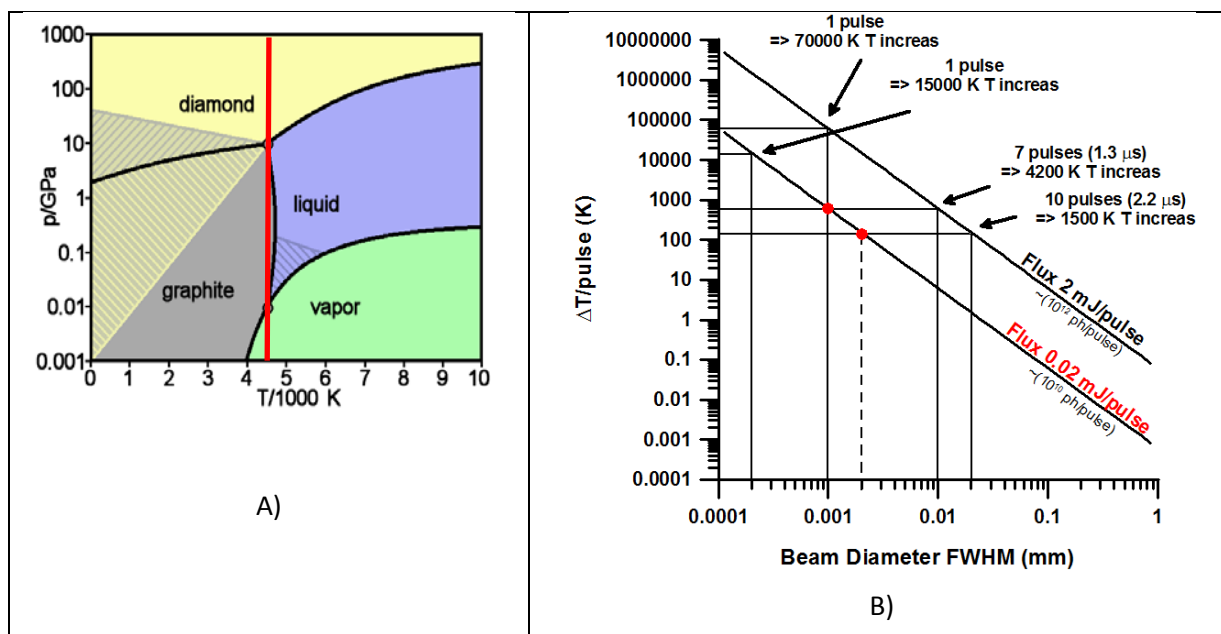


Figure 10: A) Phase diagram of diamond indicating that above 4500 K diamond will either sublimate at ambient pressure or melt at high-pressures. B) Displays the temperature increase as a function of beam size and flux per pulse calculated for 25 keV (isochoric heating) in the two diamond anvils (4.2 mm thickness). Flux of 2 mJ/pulse is equivalent to the maximum expected photons for the European XFEL at the HED instrument. The flux of 0.02 mJ/pulse represents the maximum flux necessary for collecting a diffraction image of 20 μm thick iron sample compressed in a DAC. This calculation is based on Blome et al. (2005) and indicates that one can expect at 0.02 mJ/pulse of the order of 10^3 ph/sec. From this conservative estimation we expect that the DAC heats up to 1500 K when illuminating it with 10 pulses of a 2 μm^2 beam. At 1 μm one will reach the threshold for the destruction of the diamond anvils after 7 pulses. These calculations do not consider the fact that the diamonds are very good thermal conductors so that they will dissipate the heat deposited in a very small area very quickly. Thermal conductivity calculations show that the temperature in a standard diamond anvil will drop from 15000 K in 100 ns. Due to this dissipation we expect that one can deposit significantly more XFEL pulses in the diamond anvils before they show damage.

Estimating the damage threshold for the diamond anvils and the sample has shown to be a major concern for the DAC setup at the HED instrument of the European XFEL. We have calculated the heating that a diamond will experience when exposed to a XFEL beam of 2 mJ/pulse ($\sim 10^{12}$ ph/pulse) and 0.02 mJ/pulse ($\sim 10^{10}$ ph/pulse) as function of beam size at 25 keV (Fig. 10). These calculations show clearly that a 1 μm beam at 2 mJ/pulse and a 100 nm beam at 0.02 mJ/pulse will heat the sample to 70000 and 15000 K/pulse, respectively, and thus destroy the anvils in one shot. On the other hand the 1 or 2 μm beam size at 0.02 mJ/pulse will heat the diamond anvils only by ~ 600 and 150 K/pulse, respectively. Assuming the heat is accumulated during each pulse this would enable the deposition of 7 pulses with 1 μm beam size at 0.02 mJ/pulse before the

diamond would reach 4200 K, at which temperature at high pressure the diamonds would melt. When using a 2 μm beam one will be able to deposit 10 pulses and only reach a temperature of 1500 K. However, we note here that at a 100 fs pulse length the maximum pulse energy will be 0.8 mJ/pulse. Thus, above estimates are rather on the conservative side, also because thermal conductivity models (Fig. 11) indicate that the high thermal conductivity of diamond results in heat dissipation in between the pulses, thus enabling the deposition of many more pulses before the diamond heats up significantly and reach the damage threshold. In fact the detailed heat transports calculations illustrated in Fig. 11 indicate that the diamonds heat up to 600 K and cools down to room temperatures when using a 2.5 GW power beam at 20 keV incident beam energy (0.2 mJ/pulse, see also Fig. 1 from Medvedev et al. 2013). This means that the diamonds will survive the maximum flux from the XFEL with a 100 fs pulse length.

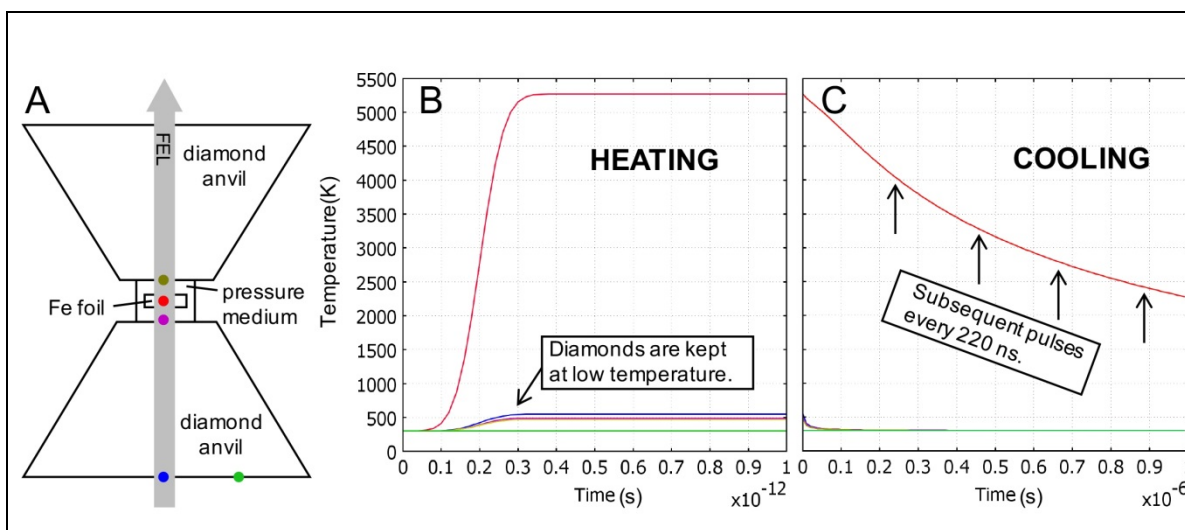


Figure 11 A) Simulation of heating/cooling of a DAC after a 100 fs x-ray pulse. Also shown in this simulation is the development of the thermal evolution of an 5 μm thick iron foil placed in the insulation medium of LiF. The x-ray beam is focused to 5 μm in diameter. The power is 2.5 GW at 20 keV as specified in the CDR of HED (2.5 mJ/pulse). Absorption length of the x-rays at this energy in the diamonds is 11 mm. B) Plots show temperature history at various points of the DAC assembly as well as the iron sample. The maximum temperature in the diamonds (600 K, middle panel) is reached when first entering the upstream diamond anvil after about 300 fs of peak pulse arrival. C) Cooling to room temperature in the diamond is expected after 100 ns (right panel) while the iron sample will heat up to 5300 K, not cool down significantly from one to the next pulse (220 ns) but accumulatively heated. This means that at 2.5 GW the sample will cool down from 5500 K to some 2000 K, i.e. if isochoric heating is not desired one need to reduce the bunch charge further through attenuation, increase the size of the beam or prevent the insulation of the sample.

Finally, the question that remains is if we can collect enough scattering signal at the thinnest sample anticipated. Let us consider a 2 μm thick foil which we estimated in the previous section to give us a scattering signal of 10^2 ph/(pulse, pixel) when the incident beam contains 10^{10} ph/pulse. Considering, e.g. the Perkin Elmer detectors that requires 80 ph/pulse to be above the background, we can anticipate that we will get just enough scattering signal in one pulse. This will be the most extreme case and one may opt to collect a diffraction image during 2 pulses to



increase the statistics, still resulting in approximately 12 diffraction images over a 6 μ s long heating pulse (see section 3.3. and Fig. 5) while temperature will stay relatively low. However, when using an GaAs AGIPD detector as proposed for this setup (see section 12.3) one might be able to lower the fluency even further (by a factor of almost 100) because the AGIPD detector has single photon counting capability and thus no background.

6. Sample Environment Requirements (Vacuum Chamber)

Above discussion makes it clear that the interaction between the x-ray beam of the XFEL and the diamond anvils will lead to a substantial heating depending on the beam size that eventually will result in graphitization of the anvils. Furthermore, the AGIPD detector foreseen for the very fast heating experiments has to be operated in vacuum because of condensation issues related to the cooling of the detector. If one would operate the AGIPD in air, a vacuum interface in front of the detector would be necessary (e.g. diamond window) that would result in significant parasitic scattering on the detector. A similar effect can be expected from air scattering at 25 keV beam energy. This needs to be avoided in order to detect the scattering signal on the detector.

For the above reasons we have decided to place the DAC setup in a small vacuum chamber that should be able to reach a vacuum of $10^{-4} - 10^{-5}$ mbar in ~ 10 minutes (exact pump down time to be determined in the TDR) that we know from experiments at the ECB with resistive heated DAC in vacuum, will be sufficient to protect all heated component from oxidation. In the final consequence this means that all components such as motors, etc. have to be vacuum compatible. Since we need a 500 mm flange to be able to enter the AGIPD detector into the vacuum chamber (see section 10), the minimum dimensions are fixed and because of stability issues of such chamber a round or octagonal shape is preferable. During the discussion concerning the chamber the idea was born that this small chamber could be compatible or very similar to that chamber currently been produced for laser shock compression experiments at the Dynamic Compression Sector (DCS) at the Advanced Photon Source (APS) Argonne National Laboratory (ANL), Chicago, US. This idea found support from the SAC, TAC and Management Board of HIBEF and it was recommended to further investigate during the conceptual design phase if the combination of a small laser shock setup similar to that of the DCS and the vacuum chamber for the DAC is feasible. A detailed discussion of the advantages and disadvantages of such scenario can be found at the end of the CDR in section 16. Thus, in the following we have taken the conceptual design of the DCS chamber and have adopted it for the needs of the DAC setup at the HED instrument.



Based on the information that is available to us at the moment the DCS chamber mimics a sphere with a diameter of ca. 1 m (36") that consists of three parts, a central cylindrical part and 2 half spheres all of which are populated with 14" flanges in octagonal geometry (Fig. 12). The plan of the DCS is to flange different analytical units to this chamber. The laser for shock compression is introduced from the side through the middle of the support of the vacuum chamber, deflected to the side and upwards via a "laser arm" and reverted through one of the 36" flanges into the chamber. Details of the beam path for the shock laser (which would be the diode laser from the UK consortium portion of HIBEF) has been worked out in the CDR for shock compression experiments at the HED instrument. The support column of the vacuum chamber that carries the laser in it offers three degrees of freedom: horizontal, vertical translation and a rotation. These permit the variation of the laser shock direction with respect to the x-ray beam via the rotation and alignment of the laser interaction point with the x-ray beam via horizontal and vertical translation. These three degrees of freedom are moving the vacuum chamber and a sample support plate inside the chamber. In order to reduce any vibrations originating from the vacuum pumps attached to the vacuum chamber the sample support plate is detached from the vacuum chamber and sits on three columns that are grounded on the rotation but are detached from the vertical translation. Thus, the sample height of the plate inside the chamber is fixed in height, but can be rotated and aligned horizontally to the beam. The sample support plate is not grounded on the floor as in the case of the main chamber of the HED instrument as far as we can tell from the information we have at the moment. We have used the above information to create a chamber that has flange opening identical to those of the DCS chamber but with the following modifications (Fig. 12):

- a) In order to insert a 1 M type AGIPD detector (see below) one of the 14" flanges were enlarged to 500 mm ISO flanges.
- b) To provide different HE laser vs. x-ray beam geometries (22.5, 45, 67.5, 90, 112.5° see shock compression CDR) one side of laser was equipped with 200 mm flanges.
- c) The incorporation of the 500 mm and 200 mm ISO flanges for the AGIPD detector and the HE laser, made it necessary to enlarge the overall diameter of the chamber to 1200 mm in comparison to the ca. 36" of the DCS chamber.
- d) The decoupling of the sample plate prevents us from aligning the DACs with the existing translation system so that we added an alignment system with 5 degrees of freedom on top of the sample support plate as it is common in most high-pressure beamlines working with DAC's (see next chapter).

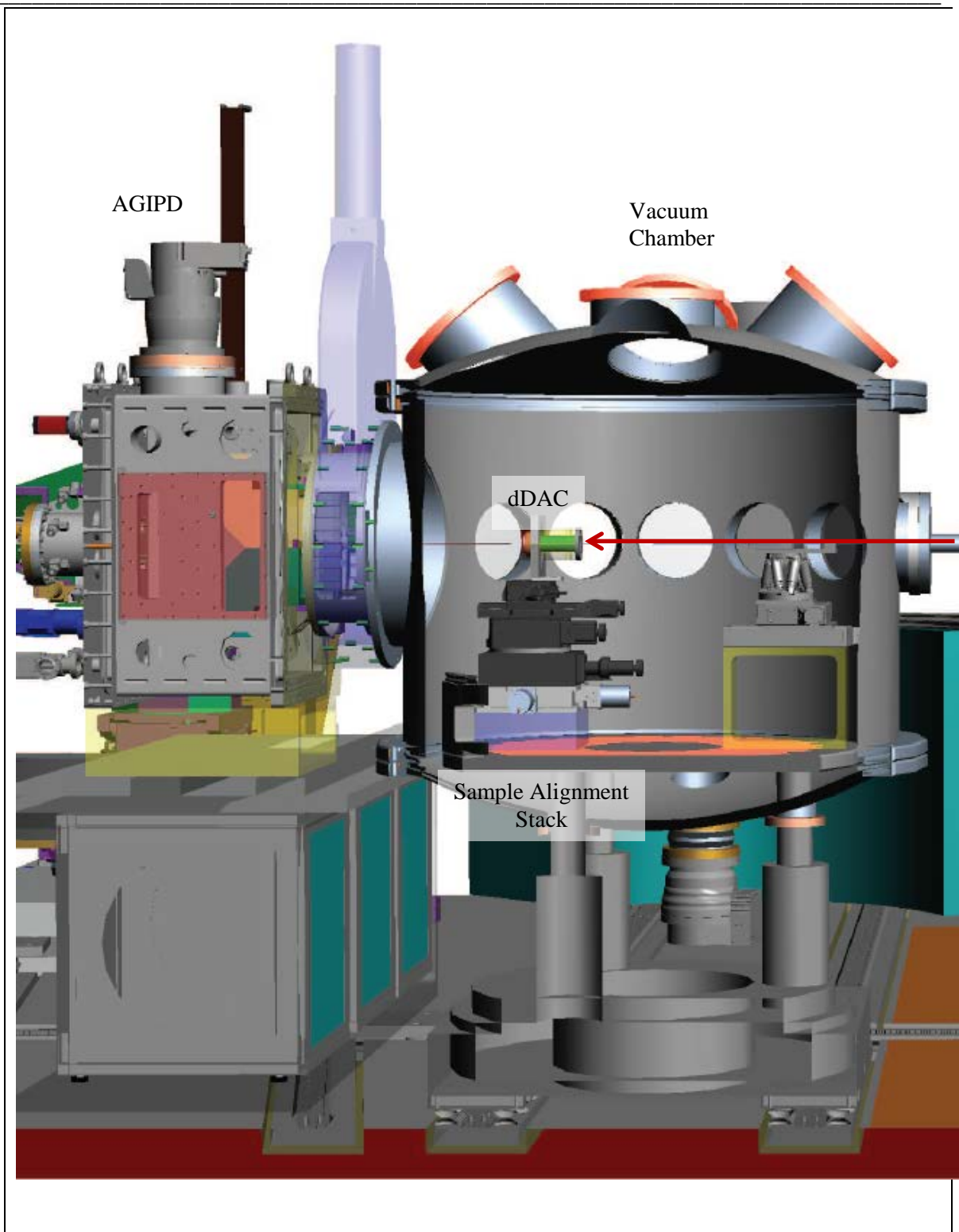


Figure 12: 3D representation of the vacuum chamber for the DAC setup that may also be used for laser shock experiments similar to the vacuum chamber of the DCS at the APS. DAC sample alignment stack is positioned 300 mm from the center of the chamber shown with a dDAC from the ECB. This enables coverage of $2\theta = \pm 45^\circ$ at a Sample to Detector Distance (SDD) of 200 mm and would cover the opening of a standard Boehler Almax DAC (see also Fig 14). It also allows the positioning of a nano focusing setup described in section 4.3 within the vacuum chamber. The chamber is positioned on a rail system enabling movement of the chamber in and out of the beam for easy installation and break down of the experimental setup. Downstream shows the AGIPD detector model build for the MID instrument at the European XFEL. The GaAs version of the AGIPD detector for HED will be similar (see section 12).

Details of the vibrational detachments from the vacuum chamber and alignment system below have to be worked out in the technical design report (TDR) after a decision has been made that the vacuum chambers for laser shock and DACs will be combined and we have more details from the DCS about their chamber.

7. Sample Positioning Requirements

For pre-alignment one may use an online microscope/ruby pressure measurement system or the laser heating imaging system (see section 9). The final positioning of the sample in the DACs with respect to the XFEL beam is best performed with the attenuated beam while scanning the DAC. Because of the small sample in the case of the dsDAC experiments we have foreseen a positioning system with at least 100 nm positioning accuracy and five degrees of freedom as it is custom at high-pressure beamlines working with DACs (see Liermann et al. 2015). Table 6 lists the positioning components that have been selected with some critical specifications. The sample alignment stack in the vacuum chamber is positioned 300 mm downstream from the center of the chamber. This enables coverage of $2\theta = +/-45^\circ$ with an AGIPD detector at a Sample to Detector Distance (SDD) of 200 mm and would cover the opening of a standard Boehler Almax DAC (see also Fig 13). It also enables the positioning of a nano focusing setup described in section 4.3 within the vacuum chamber.

Table 6: Positioning components for alignment of the DAC into the XFEL beam at the HED. All components are vacuum compatible (HV).

Function	Alignment of Rotation Center into XFEL beam	Vertical Alignment	Rotation	Sample alignment into rotation center
Component	Huber XY 5102.30	Micos NPE-200	Micos PRS-200	Micos LS-110
Weight (kg)	15	9.2	8	2.7
Load Capacity (kg)	200	30	50	10
Travel (mm)	15	13	360 degrees	26
Resolution (μm)	0.1	0.05	0.001 degrees	0.05
Bi-directional Repeatability (μm)	0.1	+/- 0.04	+/- 0.001 degrees	0.1
Wobble (μrad)	n.a.	n.a.	± 17.5	n.a.

8. Sample Heating and Temperature Determination in the DAC

Heating the sample at high pressure in the DAC will be one of the major technical advancement that will lead to significant new scientific findings. This is particular true for the dsDAC because at high temperature, ultra-high pressures are difficult to maintain for more than a few ms, too short to collect a diffraction image at a 3rd generation source. Thus, heating the sample is essential part of the project for the dsDAC but also for the dDAC that are depending on the high repetition rate of the European XFEL.



There are three types of heating that one may employ in the DAC: isochoric heating, pulse laser heating and resistive heating. The latter two are employed at 3rd generation light sources while the isochoric heating is somewhat new to the static high-pressure community. Neither pulsed laser heating nor the resistive heating techniques are covered by the HIBEF funding but will be contributed through 3rd party funding and in kind contributions. Since isochoric heating is a byproduct of the XFEL x-ray beam (see Fig. 11), one may wonder why not employing exclusively isochoric heating for the creation of high temperatures. The reason is simple, the sample cannot be heated prior to the x-ray arrival and the area that is being heated (e.g., 1 μm^2) is very small, creating a large temperature gradient in the sample between the two highly conductive diamond anvils. For certain experiments we will try to explore and employ isochoric heating but for the large portion of the heated high pressure work we prefer a more homogenous way of heating, i.e. pulsed laser heating (5 μm diameter or larger) and resistive heating (sample, gasket and anvils). Below we provide a quick overview of the envisioned heating techniques.

8.1. Isochoric Heating

Isochoric heating is a side product of employing a very intensely focused x-ray beam at the HED instrument of the European XFEL. Using the same approach as in the diamond damage threshold discussion we try to estimate how much the XFEL beam would heat the sample. Fig. 13 indicates that 1 μm beam at 2 mJ/pulse will heat a 5 micron foil in single shot to 30000 K and even at 0.2 mJ/pulse (still enough to get a diffraction image, see section 4.4) reach 5300 K (see Fig. 11) in one pulse assuming that the heat is not dissipating. The latter assumption is not realistic since the sample, especially in the case of the dsDAC is held between the highly conducting anvils. Thus, if the sample is in direct contact with the diamonds temperature on the sample in between pulses (222 ns) will dissipate because of the diamonds high heat conduction and thus have only a minor effect on the overall temperature of the sample. On the other hand, if one would insulate the sample from the diamonds (as is custom during laser heating) the sample will not cool down as quickly and one might be able to use isochoric heating to steadily heat the sample while collecting diffraction images after each heating pulse. Detailed Finite Element (FE) heat conduction simulations shown in Fig. 11 for the case of heating a 5 μm thick foil of iron at 20 keV incident beam energy and 2.5 GW power (corresponding to 2.5 mJ/pulse) indicate that iron which is properly isolated with e.g. LiF temperatures can reach 5300 k in one pulse only to 4000 K before the next pulse arrives. Thus, one may use this to continuously heat the sample. Further heat transfer calculations are necessary to estimate the thermal gradient for

the case that you are only heating a 5 μm spot, rather than heating larger areas of the sample as is custom with CW and pulse laser heating.

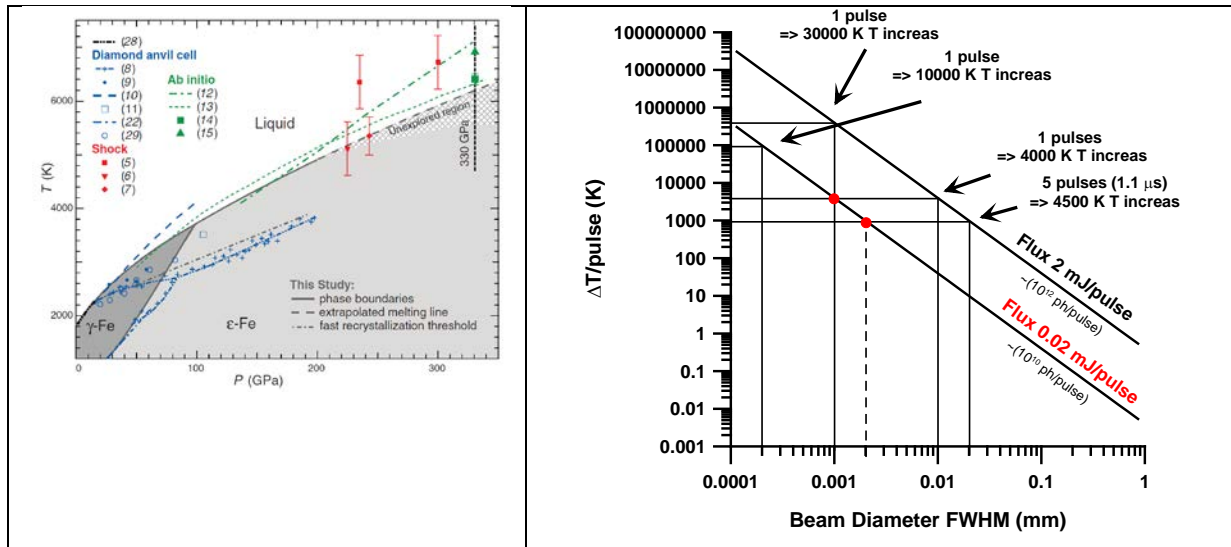


Figure 13: A) Phase diagram of iron as a function of temperature and pressure (from Anzellini et al. 2013). B) Displays the temperature increase as a function of beam size and flux per pulse calculated for 25 keV (isochoric heating) of a 5 μm thick iron foil. The plot shows that the sample will heat up very quickly. However, these calculations do not consider the dissipation of the heat through the diamonds that will be in direct contact with the sample in the case of the dsDAC. Because of the high heat conductivity of diamond the sample will stay a lot cooler and many more shots can be deposited in the sample without significant heating.

8.2. Pulsed Infrared Laser Heating

Pulsed infrared laser heating is becoming a technique in the DAC community that is being considered more and more for flash laser heating or pump and probe experiments (e.g., Narygina et al. 2011, Kuppenko et al. 2015). The technique becomes particularly interesting when combining it with the high-flux and -repetitive x-ray beam available at the HED instrument of the European XFEL as pointed out in section 3.3. and Fig. 5. Our collaborators from Bayreuth have applied for 3rd party funding to build such a laser heating setup that will be able to also measure temperatures at the maximum repetition rate available at the HED instrument (4.5 MHz) employing streak cameras. Fig. 14 depicts the conceptual setup of a double sided pulsed laser heating system in the DAC vacuum chamber. Note that the mirrors cannot be in the x-ray beam of the XFEL because it would destroy them. In order to minimize the thermal gradient in the sample it is foreseen to employ π -shapers (Prakapenka et al., 2008). Details of the system have to be worked out during the TDR phase.

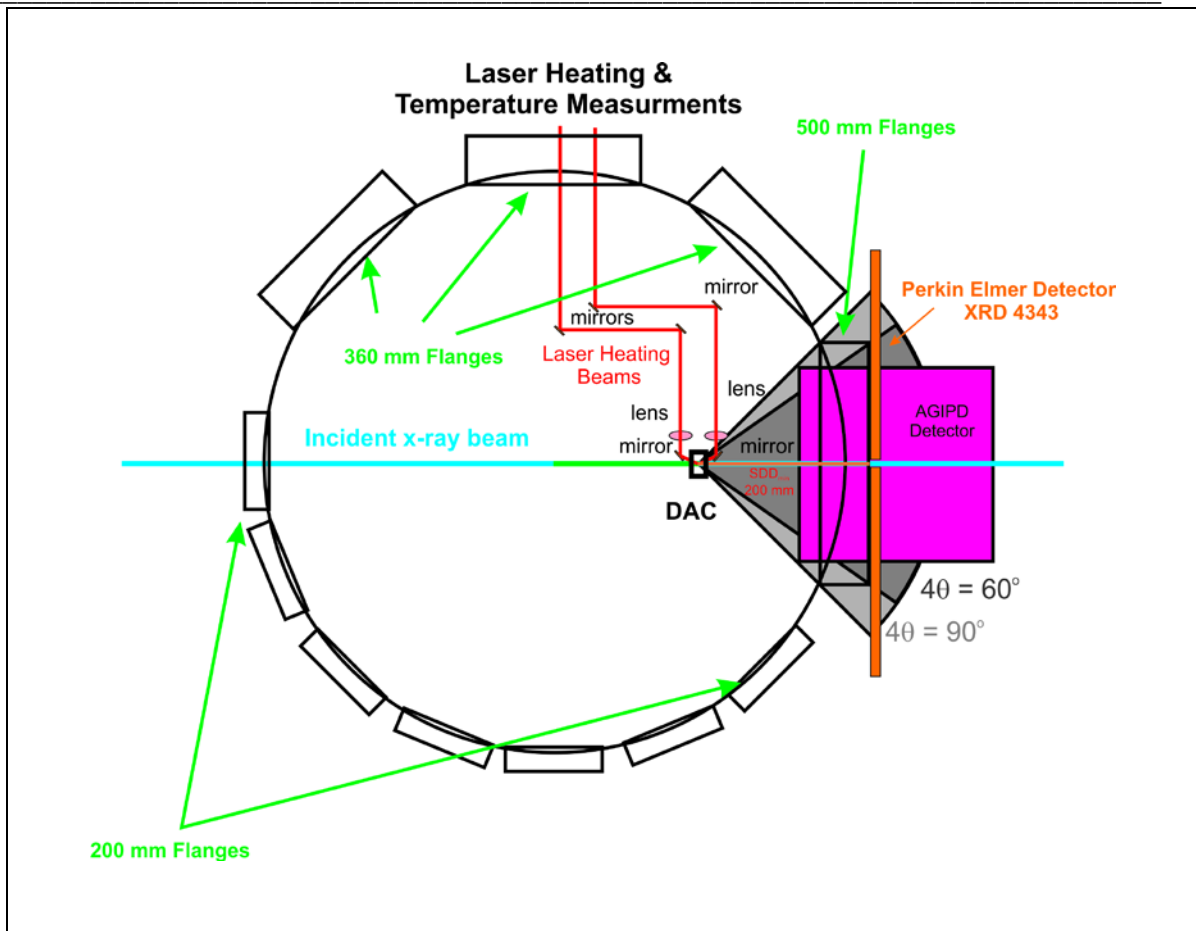


Figure 14: Conceptual setup of a double sided pulsed infrared laser heating system to heat samples in the dsDAC or the dDAC. The sketch also indicates that with the AGIPD detector we can cover an opening angle of $2\theta = \pm 45^\circ$ and $4\theta = \pm 30^\circ$ with the AGIPD and with the Perkin Elmer Detectors XRD 4343 ct (outside the vacuum), respectively.

8.3. Resistive Heating

Resistive heating with wire or graphite resistive heaters (see Fig. 15) is a standard technique at high pressure beamline of 3rd generation light sources such as the ECB (Liermann et al. 2015) to create temperatures up to 2000 K. It is foreseen to make both techniques available as an in kind contribution from the ECB at PETRA III, DESY. This includes ultra-stable power supplies and thermocouple read out electronics. Implementation will require also adaptation of the heating techniques to the dDACs. Application to the dsDAC is also foreseen and might be used to characterize the yield strength and weakening of the second stage anvils as described by Dubrovinskaia et al. (2016).

9. Pressure Measurement in the DAC

For the pre-alignment and visualization of the sample in the dDAC as well as for initial pressure measurements it will be very desirable to position an online microscope with ruby fluorescence measurement capability upstream from the sample position, looking down stream. Such

system is standard equipment at all beamline at 3rd generation light sources that perform high pressure research (e.g. Liermann et al. 2015). Such system could be also equipped with objective that lets the x-ray beam pass thus enabling observation of the sample during the experiment.

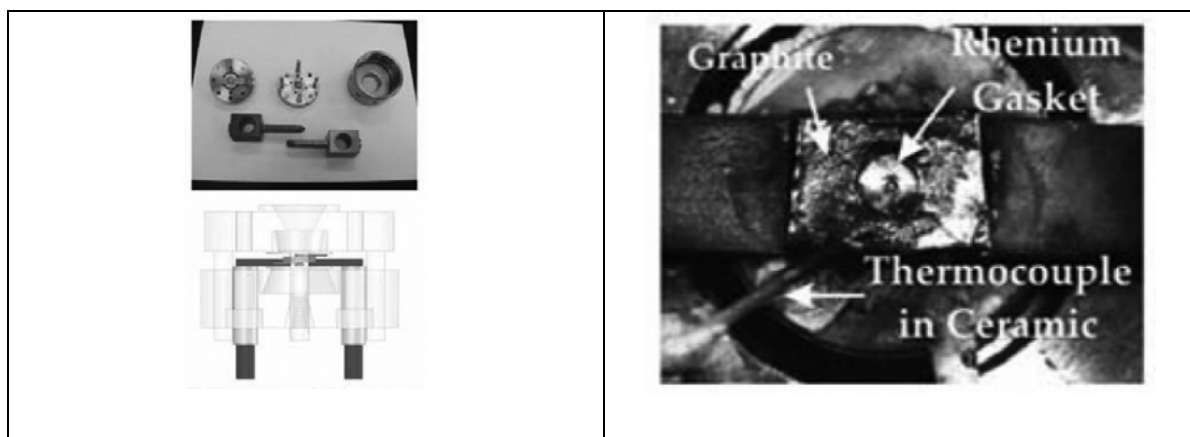


Figure 15: Graphite resistive heating setup in a four pin DAC (from Liermann 2015).

10. Cleanup Slits (pinhole)

The cleanup slit is an essential part of any diffraction setup in the DAC and needs to be positioned as close to the sample as possible, i.e. ideally directly in front of the upstream diamond anvil. This is necessary because the incident beam always shows a tail that scatters at the edges of the sample containing gasket or it convolutes the pressure measurement on a very small sample such as that present in the dsDAC. Typically the cleanup slit system consists of the pinhole in a high Z and thick metal such as Pt or W. At the ECB we use a 5-10 μm pinhole in a 0.25 - 1 mm thick Pt foil depending on the energy (penetration depth) of the X-ray beam. Based on the above experience we propose for the double-stage DAC (dsDAC) a 1 μm^2 beam (FWHM) that would require a pinhole (cleanup) with a diameter of 2-5 μm positioned as close as possible to the sample (directly on the back size of the diamond anvil). For dynamic DAC (dDAC) experiments the beam size and the sample relaxes with 10–40 μm^2 (FWHM) and thus requiring only a radius of the pinhole of 40–80 μm . The location of the pinhole with respect to the sample is also relaxed, i.e. it can be as much as 150mm away. This is also true for all laser heated experiments because the laser has to be guided to the sample at an angle and it requires some additional space.

Table 7: Proposed clean-up slit sizes for different DAC samples and proposed X-ray beam sizes.

Sample Size (μm)	Focused Beam Size (FWHM, μm)	Clean-up slit size (FWHM, μm)
1	1	5
20	20	40
40	40	80

For the implementation of such a clean-up slit system we first look at the slit system foreseen for the HED instrument and then make use of their experience to design a slit system close to the DACs. The HED instrument plans a high power slit systems at the entrance of the optics hutch of HED instrument. This slit system is water-cooled and consists of a 5mm TaC blades that are deposited upstream with 75mm of B_4C . Here the B_4C acts as an absorber of the incoming beam and the TaC as blocking device. This slit system can cope with the full repetition rate of 4.5MHz for half a bunch train of the XFEL. However, it cannot be fully closed during the entire bunch train and thus is only meant to slit down fractions of the incident beam at the high-repetition rate experiments (for low repetition rate experiments and shot on demand the requirements are somewhat relaxed). The XFEL beam is further shaped in the optics hutch by CRL lenses and then potentially interacts with attenuator foils, a diamond grating, a timing tool and a spectrometer. All these devices create parasitic scattering. In order to clean up the beam from this parasitic scattering a second slit system is foreseen, 2m in front of the sample in IC1 and 4m from IC2. This slit systems consists of two components, a low Z slit system and a subsequent high Z slit system. Because sharp edges are known to cause significant scattering, the low Z slit system will consist of a soft edge by means of a rod made of Si_3N_4 with a diameter of 3mm mounted on a 2mm Ta blade. This results in a gradual change of the transmission of the beam (Figure 16). Directly downstream, a high Z slit system will be installed consisting of 4mm thick TaC blades protected by a 6mm thick B_4C layer mounted on the upstream side. The B_4C layer is about one tenth of the thickness of the high-power slit system: following the assumption, that only 10 % of the incoming beam are scattered at this slit system, this is considered sufficient. Finally, there need to be a specific cleanup slits for DAC experiments closer to the sample. Because of the large amount of heat that will be deposited into the cleanup slit (pinhole) when cutting the tails we decided for the moment on the following design of the cleanup slit:

The pinhole will consist of a layer of B_4C that is bonded to a foil of TaC. Because pinholes of 5 μm can only be laser cut into 1mm or thinner assemblies we propose a sandwich of 0.4 mm TaC and 0.6 mm B_4C . This will result in a factor 10 more absorption than necessary according the absorption length of TaC at 25 keV and a factor of 0.03mm of the absorption length of B_4C (Fig. 17).

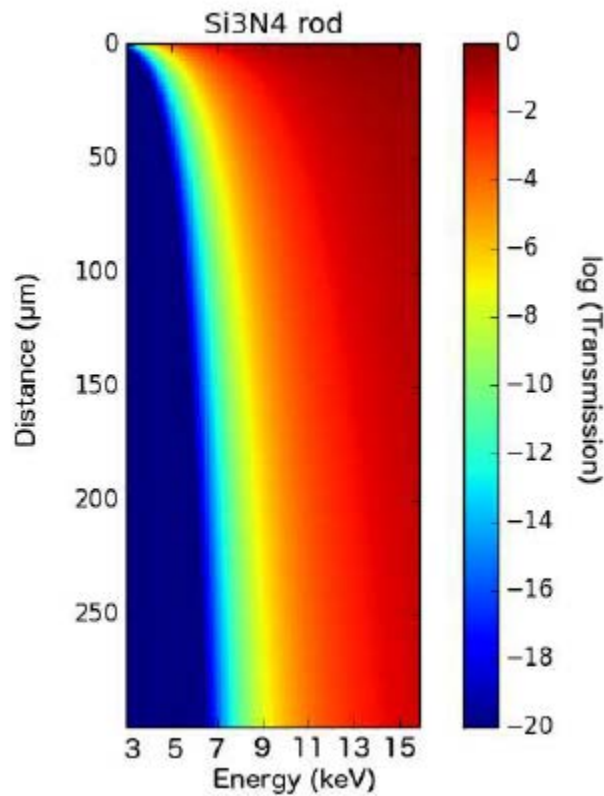


Figure 16: Transmission of the first 300 μm of a Si_3N_4 rod blade mounted on a 2 mm thick Ta blade. The rod has a diameter of 3 mm.

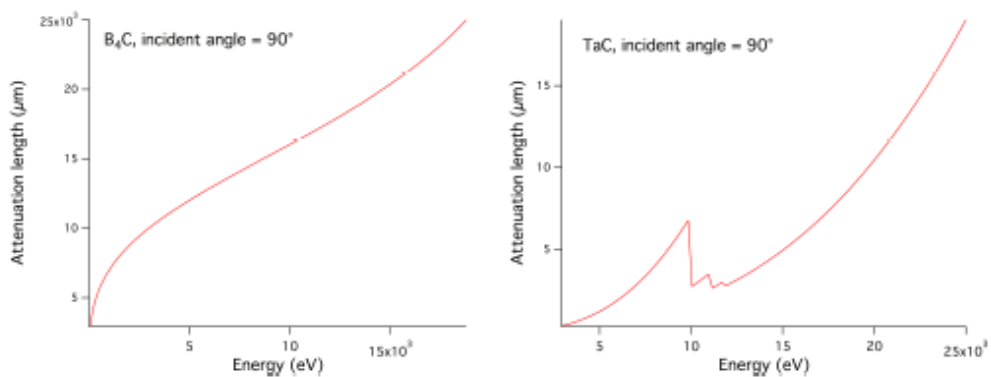


Figure 17: Attenuation length for B_4C (left) and TaC (right). At 1012 photons per pulse we need twice the attenuation length to reduce the transmitted photons to a manageable amount. This means we would need at least a 40 μm thick foil of TaC with a 20 mm B_4C layer. However, because only small parts of the beam are expected to hit the pinhole and 20 mm thick pinholes are difficult to align, we decide for an 0.4 mm thick foil of TaC bonded to a 0.6 mm B_4C layer positioned upstream. This will give us a factor 10 thicker TaC absorber than necessary.



11. Beam Stop and Beam Transport after Sample

The beam stop for a XFEL beam is an essential task for every instrument and has been realized at the HED instrument at the end of the experimental hutch through a massive block of B_4C located in vacuum that absorbs the primary beam at maximum flux available and maximum repetition rate. We have considered implementing a beam stop between the DAC and the detector in order to be able to employ detectors that do not offer a hole to let the x-ray beam pass. However, after considering the thickness of such a beam stop and the fact that it will most likely create massive parasitic scattering in front of the detectors we have decided to use the beam stop at the end of the HED instrument and guide the beam through a hole in the detector or a gap when using multiple continuous sensor detectors. This limits the application of detectors employed at the DAC setup. For example the AGIPD detector is inherently operating in vacuum and has a hole for letting the primary beam pass and thus is ideally suited for this DAC setup. Other detectors, such as the amorphous silicon detectors from Perking Elmer (e.g. XRD 4343 ct) consist of a continuous sensor area so that they may only be employed when tailing two or more detectors together, so that the beam may pass the detector at the edges. Both scenarios and the expected 2θ angles are indicated in Fig. 14. In any case the, after the x-ray beam passed through or by the edge of the detector the primary beam has to be further transported in a small vacuum tube towards the beam stop at the end of the HED hutch.

12. Detector Requirements and Instrumental Resolution

Detectors recording diffraction images of samples compressed in the dDAC or dsDAC ideally at the repetition rate of the European XFEL are a challenging task. In addition the detectors should operate in vacuum, have a hole for passing the incident beam to the beam stop at the end of the hutch of the HED instrument, have a Quantum Efficiency (QE) of almost 100 % at 25 keV, cover an as large portion of reciprocal space as possible (at least $Q = 9.7 \text{ \AA}^{-1}$ to cover a $4\theta = 90^\circ$ opening in a DAC) and an instrumental resolution as high as possible. The GaAs version of the Adaptive Gain Integrating Pixel Detector (AGIPD) detector proposed in this CDR will ultimately be able to meet most of these requirements, except a really good instrumental resolution (see section 12.4). However, at the moment only a Silicon version of the AGIPD detector has been constructed, requiring engineering runs and prototype building of the GaAs version prior to construction and installation of the detector at the HED instrument. In addition, funding for the development of such a detector will not be available until 2018 when we can foresee already first experiments at the HED instrument. This means that we have to come up with intermediate solutions (staged detector approach) to be able to

test the DAC setup in the vacuum chamber as well as to evaluate the experimental concepts to conduct DAC experiments described above.

Table 8: Important detector specifications of the selected detectors for comparison.

Detector	Chip	DQE (@ 25 keV)	Pixel Size (mm ²)	Dynamic Range	Active Area	Frame Rate	Vacuum Comp.	Beam Hole
PE XRD 0882	CsI	48 %	0.2	16 bit	1024 × 1024	100 Hz*	No	No
Jungfrau	Si (0.5 mm)	40 %	0.075	1 to 10 ⁴ ph/pix/fr	2048 × 2048	2.4 kHz	Yes	Yes
GaAs AGIPD	GsAs (0.5 mm)	99 %	0.2	1 to 10 ⁴ ph/pix/fr	1024 × 1024	4.5 MHz	Yes	Yes

* Only for small areas of the detector (ROI) for full resolution fps is 25 Hz.

12.1. XRD a-Si Detectors from Perkin Elmer

The XRD a-Si detector series from Perkin Elmer consist of a CsI scintillator that is bonded to amorphous silicon read out chip (Table 8 for specific details). This detector has its maximum sensitivity at 60 keV with varying read-out speeds depending on size and model. The model PE XRD 1621 (0.2 mm pixel size, 15 fps) has been used extensively at 3rd generation sources such as PETRA III together with software package QXRD (G. Jennings, APS, ANL) that is optimized for x-ray diffraction experiments. At 25 keV the detector has a QE of 48% (Marshall, 2009). The major disadvantage of this detector originates from its high back ground that one has to subtract from every image (done automatically by the software QXRD) and the fact that it displays significant afterglow (ghosting) when overexposed. Nevertheless, the detector has a continuous sensor area without any gaps as in the case of tiled detectors usually employed at XFEL's (e.g. SCPads/EPix). The continuous sensor area is very attractive for performing stress/strain and texture analysis of full diffraction ring images because there are no gaps in the Debye rings. Since the AGIPD and the Jungfrau detector will not be available before the end of 2018 we like to use this detector for first experiments. We choose a newer model of the XRD series (XRD 4343 ct) that has a small rims, smaller pixel size of 0.15 mm and an afterglow that is reduced by factor of 3. In Fig. 14 we show how two of these detectors cover a 2θ range of $\pm 30^\circ$ (Fig. 14). Since the detector is vacuum incompatible it has to be positioned in front of the 500 mm flange of the DAC vacuum chamber and the flange has to be covered with an x-ray transparent window that can hold a vacuum of 10^{-4} mbar. Fig. 14 indicates that in this configuration one can expect to cover $2\theta = \pm 30^\circ \Rightarrow Q = 6.56 \text{ \AA}^{-1}$ at 25 keV (Fig. 14). The XRD 4343 ct offers a readout speed of 15 fps at full resolution and 30 fps when reading out selected areas. One may note that the detector might also be used for laser shock wave experiments with the dipole laser from the UK consortium that will operate at a maximum repetition rate of 10 Hz.

12.2. JUNGFRAU (adJUsTiNg Gain detector FoR the Aramis User station)

The Jungfrau is a detector development for SWISSFEL in collaboration with PSI and is based on the similar technology as the AGIPD and the GOTTHARD detectors employing Silicon chips. In contrast to the AGIPD this detector offers smaller pixel size which will become important for the Instrumental Resolution (IR see section 12.4). The detector operates at maximum frame rate of 2.4 kHz in continuous operation and at 1 MHz in burst mode (8-10 images) which is less than 4.5 MHz that the European XFEL and the AGIPD will operate. Nevertheless, it would be a good experimental approach to gain an intermediate time resolution before the AGIPD detector is available. The detector is vacuum compatible, can be tiled and thus could be operated similarly to the AGIPD (see section 12.3). The major reason why we are not choosing this detector for the operation of the DAC setup originates from the fact that in comparison to the proposed GaAs AGIPD detector it has half the QE (Fig. 16) and it does not operate at 4.5 MHz. In addition there is no funding in the HIBEF budget available for such a detector.

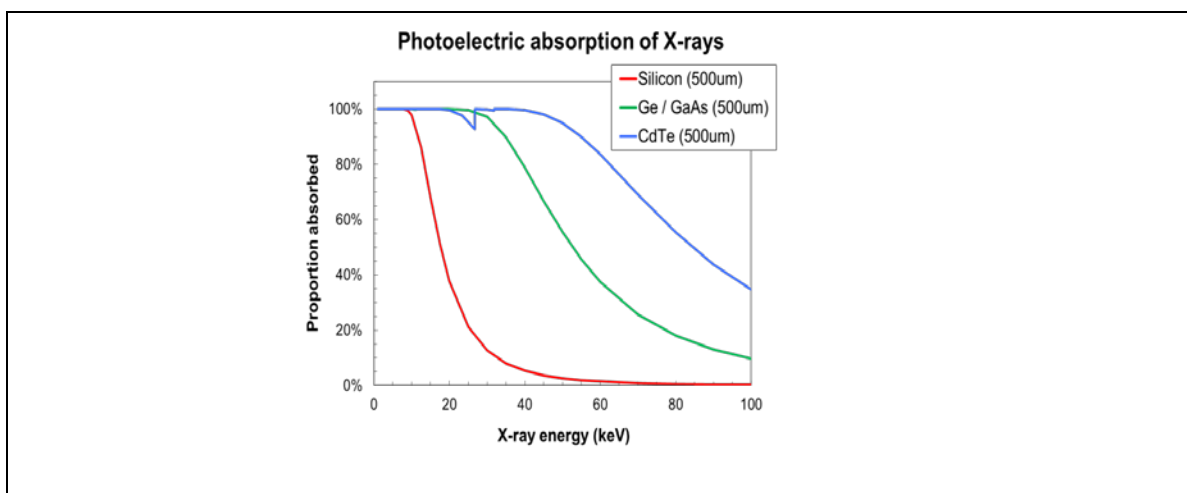


Fig. 18: X-ray photon absorption as a function of x-ray energy for the different sensor chip materials. The efficiency of the 0.5 mm GaAs is twice that of a 0.5 mm silicon chip, courtesy of D. Pennicard (FS-DS, DESY).

12.3. AGIPD (Adaptive Gain Integrating Pixel Detector)

The AGIPD is ideally suited for collecting diffraction images at the maximum repetition rate of the European XFEL. If build with a GaAs sensor it will also provide maximum QE of almost 100 % at 25 keV (Fig. 18). The detector can be tiled to let the incident beam pass and is vacuum compatible. In order to reach the $Q = 9.7 \text{ \AA}^{-1}$ to cover a $2\theta = +/-45^\circ$ opening in a DAC the SDD needs to be 200 mm. In order to achieve this distance the detector needs to be moved into the vacuum chamber. At the same time the vacuum of the detector should be maintained during the experiments and thus the detector needs to retract from the vacuum chamber and be separated through a shutter (Fig. 12) when exchanging samples. Currently it is foreseen to retract the

detector from the chamber via an in-vacuum translation (not shown in Fig. 12). It is proposed to locate the electronics necessary for a 1 M detector underneath the horizontal detector translation, as indicated in Fig. 19. This will reduce the size and thus the thickness of the 64 detectors cables significantly. The cooling oil necessary for the detector will be located away from the detector bench.

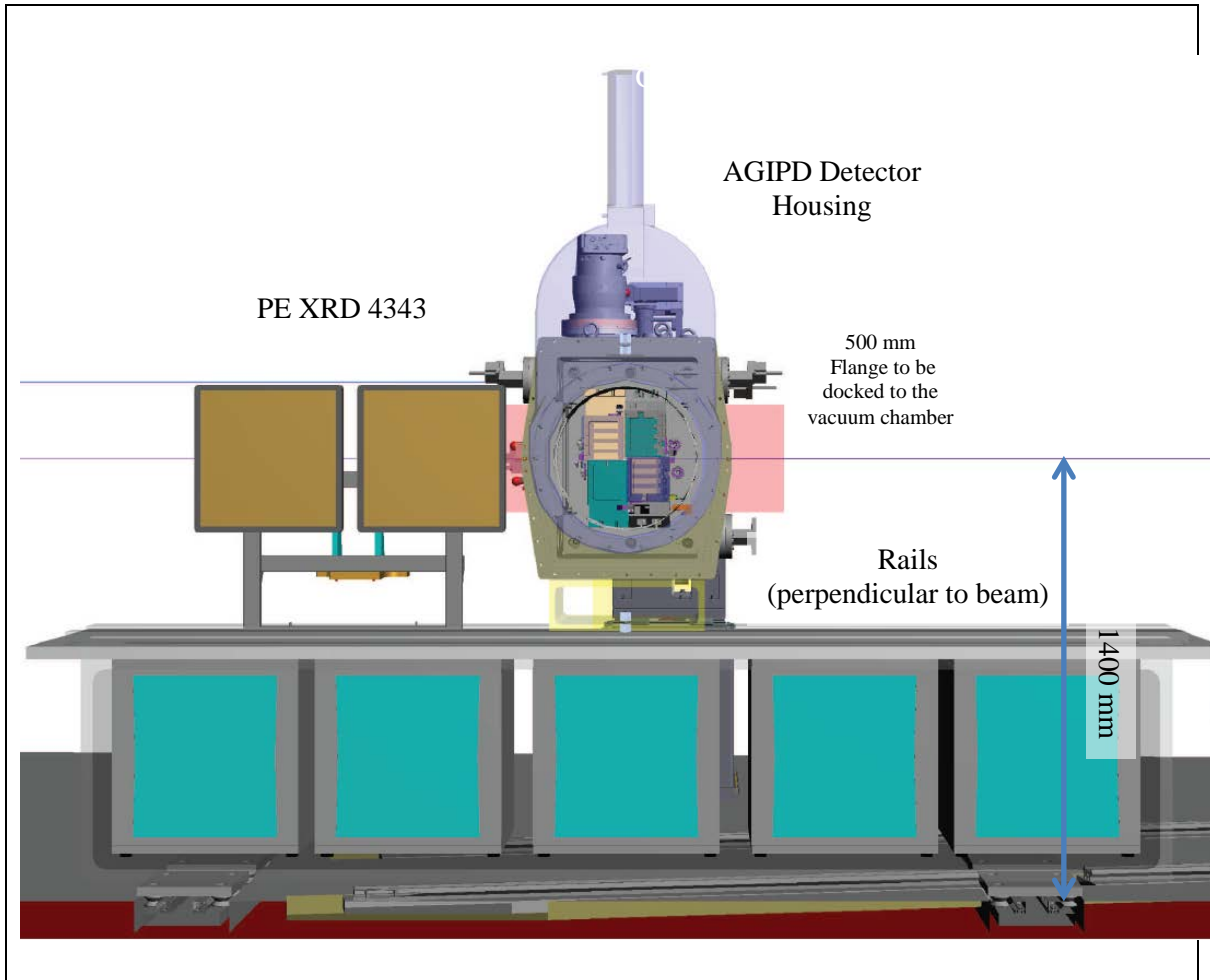


Fig. 19: Proposed location of the AGIPD and the electronic racks on the detector bench (not to scale).

12.4. Instrumental Resolution

The instrumental resolution function (IRF) for the PE XRD 4343 ct and GaAs AGIPD can be estimated from IRF of beamline P02.2 (ECB) at PETRA III (Liermann et al. 2015, Fig. 18) because x-ray beam and detector parameters are very similar to that of the ECB (25.6 keV, focus of $2 \times 2 \mu\text{m}^2$ and $\Delta E/E = 2 \times 10^{-4}$, only divergence is different). From the discussion by Liermann et al. 2015 it is evident that the dominating factor for the IRF above a SDD of 600 mm is the divergence of the beam and below this SDD the pixel size. Thus, at SDD of 400 mm (for the PE XRD 0882) to 200 mm (for the AGIPD) the pixel size of 0.2 mm will dominate the IRF of the detector and probably look similar to that of the ECB depicted in Fig. 20. The fact that the divergence of the x-ray beam

at the HED instrument will be significantly lower does probably have little influence on the IRF since the effect of the pixel size will be dominating. Thus, the IRF can only be improved when the detector has a smaller pixel size such as foreseen for the Jungfrau detector and assuming that the energy resolution of the incident beam is $\Delta E/E = 10^{-4}$. However, experience has shown that the data collected at the ECB are well suited for collecting good diffraction data of samples in the DAC.

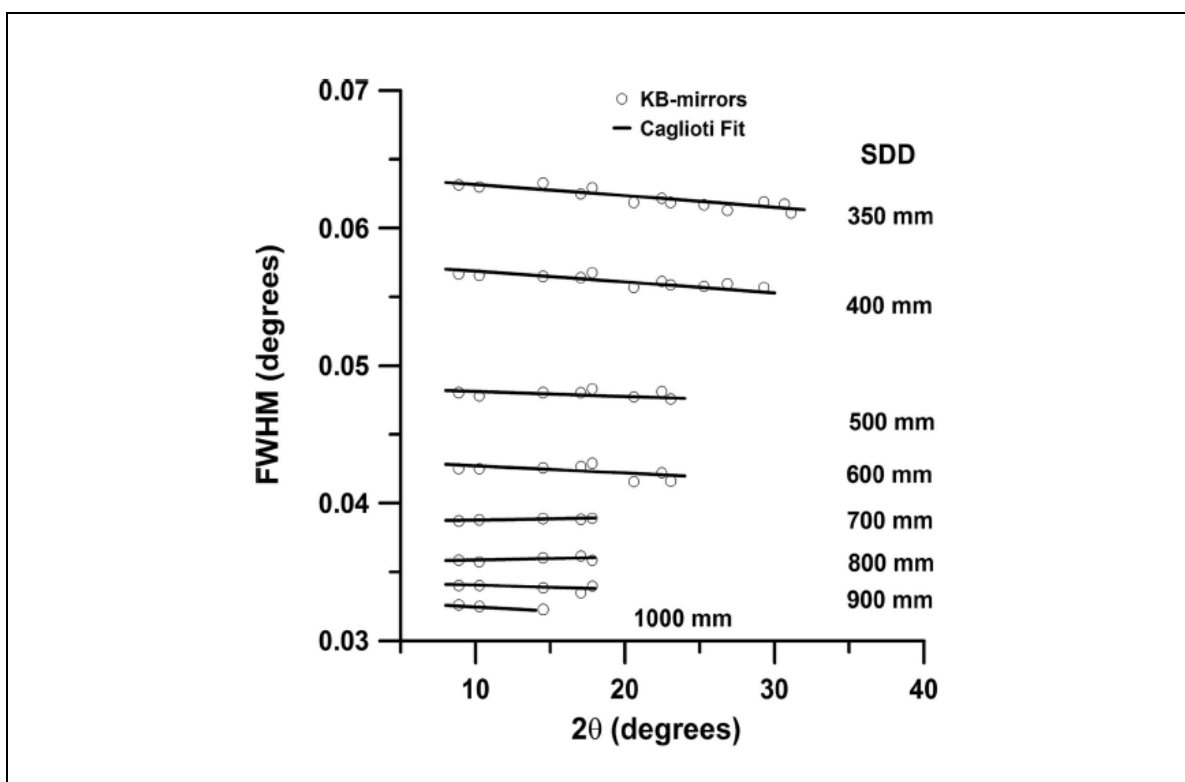


Fig. 20: Instrumental resolution function (IRF) determined from a diffraction pattern of CeO_2 (NIST standard 674) as a function of SDD at beamline P02.2 (ECB) at PETRA III collected at 25.6 keV with a focal spot of 2×2 m (FWHM) from Liermann et al. (2015). While the divergence of the beam at the HED instrument is much smaller than at the ECB the controlling factor for the IRF at SDD below 600 mm is the pixel size.

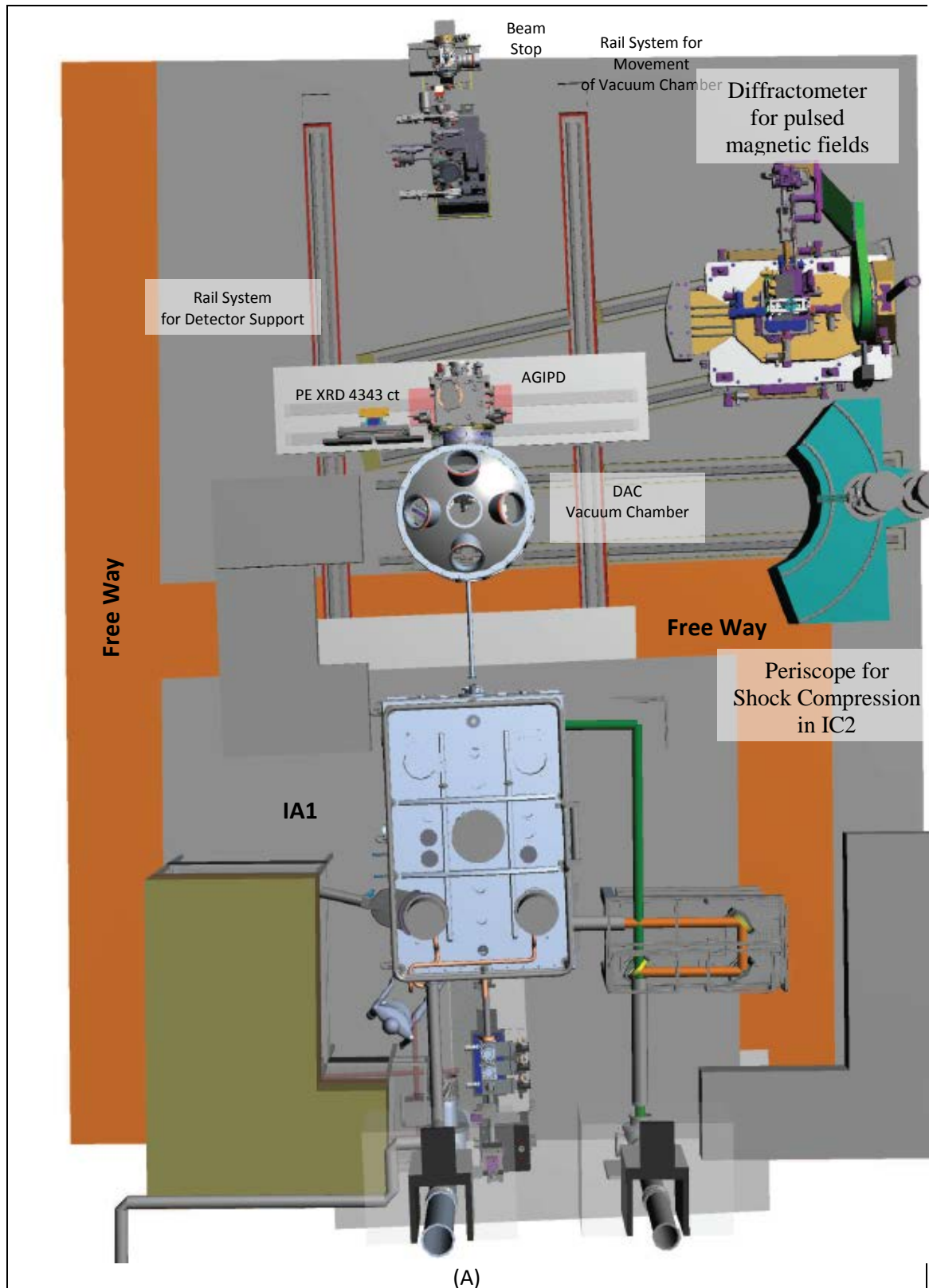
12.5. Detector Support System (together with Workpackage x-ray Instrumentation)

The above detectors should be interchangeable perpendicular to the beam and movable parallel to the beam for effective turnover of the different experiments. This means that detectors like the AGIPD and PE XRD 4343 ct need to be positioned on the downstream side of the IC1 chamber, the vacuum chamber for the DAC setup and diffractometer. In addition one might want to be able to change the SDD during the experiment reproducibly.

Among the many options discussed in the different work packages, we decided to design a detector support system (detector bench) that moves on a motorized rail system parallel and perpendicular to the beam, enabling the movement of all foreseen detectors towards IC1 and

CDR for DAC setup at HED instrument of the European XFEL
Version 2_5 (12/10/2016)

IC2_{DAC} and IA2_{diffractometer}. In this scenario the rail system for the detector bench along the beam is submerged into the floor of the HED instrumental hutch.



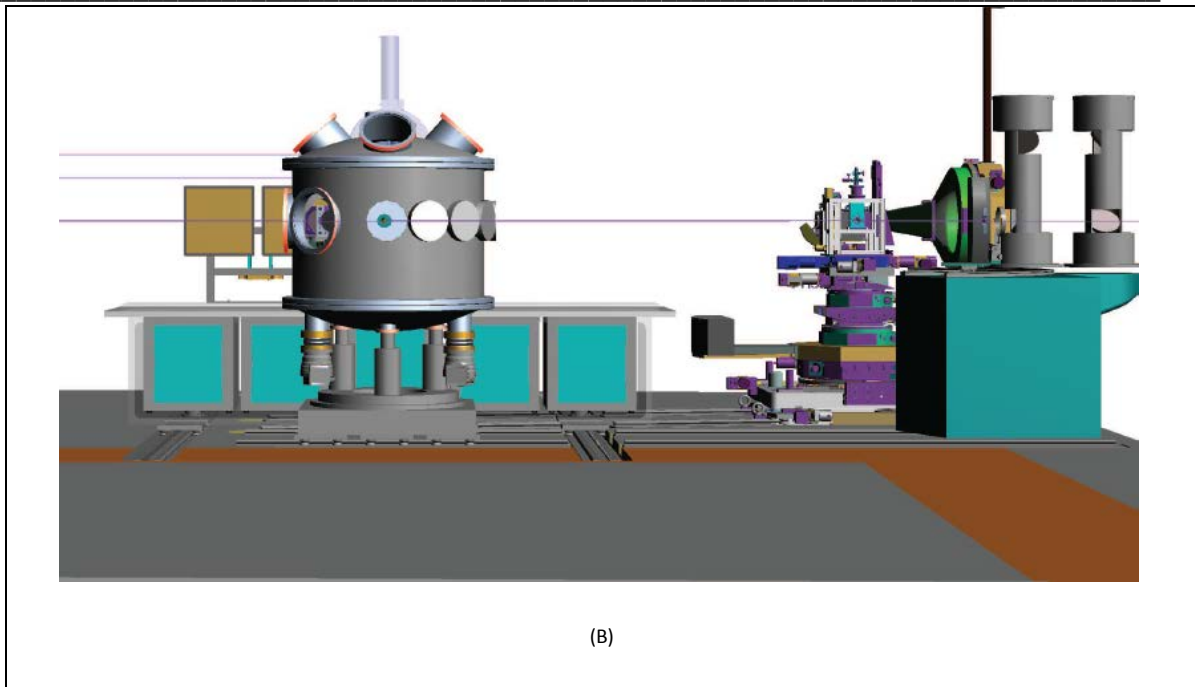


Fig. 21: Top (A) and downstream (B) view of the 3D model of the vacuum chamber for DAC experiments, the diffractometer for pulsed magnetic field experiments and the detector support system.

This has the advantage that it can be covered by e.g. metal sheet so that equipment can be moved around freely once the detector bench is retracted to the downstream side of the HED hutch. This detector rail system will be intercepted by another manually operated rail system that allows the perpendicular movement of the DAC vacuum chamber and the diffractometer for pulsed magnetic fields into the beam. These two rail systems are also submerged in the floor as the detector bench rail system. In order to cross the 2 systems one needs to remove part of the detector rail system and insert rail pieces for the other two systems. Translation of the detectors perpendicular to the beam will be accomplished by a motorized rails system ~1000 mm above the floor on top of the carriages that houses the electronic racks for the AGIPD detector.

13. Control System, Instrumentation Specific Software and Implementation

Here, we only like to mention for completeness that the control software for the operation of all motors and other equipment will neither be EPICS nor TANGO but Karabo software package specially developed for the European XFEL:

http://www.xfel.eu/news/2014/developing_a_new_software_framework_to_rein_in_a_flood_of_data.

14. Analysis Software for pressure and temperature measurements and x-ray diffraction

Diffraction images from the Perkin Elmer detector will be saved in the TIF file format while those of the AGIPD will most likely be stored in version of the HDF5 format. At the ECB we have been

developing software to analyze or convert both these file formats so they may be integrated in the form 2D images into 1D representation using either Fit2d (Hammersley et al. 1996, Hammersley, 1997) or Dioptas (Prescher and Prakapenka, 2015).

15. Preparation Laboratories

For the preparation and loading of the dynamic dDACs and dsDAC on side we require sufficient laboratory space for hosting the following instrumentation:

- Stereomicroscope for dDAC loading
- Micro manipulator with microscope for dsDAC loading
- Glove box for loading of air sensitive samples
- Vacuum oven for drying of samples
- Ruby laser measurement system for determination of pressure during indentation and initial loading
- Micro EDM and laser drilling machine for gasket preparation

16. Summary of Combined Usage of Instrumentation within HIBEF project and HED instrument

After the above considerations and discussions it seems that the DAC setup can fit well into the vacuum chamber similar to that proposed for shock compression experiments at the DCS at the APS. There are only view compromises that had to be made:

DAC setup compromises:

- a) The access to reciprocal space when using the PE XRD 4343 ct detector is limited to $2\theta = \pm 30^\circ \Rightarrow Q = 6.56 \text{ \AA}^{-1}$ at 25 keV. With a smaller chamber this access would be larger. However, this seems acceptable, considering that in the end we will only use the AGIPD detector that will provide full access this is a tolerable compromise.
- b) The DAC will not be located in the center of the vacuum chamber, which will make the pulsed laser heating path more complicated and alignment cumbersome. However, this also is only an inconvenience.
- c) We need to make sure that there is sufficient decoupling of the vacuum chamber housing from the support plate inside of the chamber. This is necessary because the focus and the sample size are in the micrometer range and hence any vibration on this scale will cause the experiment to fail. Since the design of the shock compression chamber IC2 does not foresee a

rotation and translations in the horizontal and vertical the chamber may now be positioned solidly on the floor ensuring maximum stability.

The compromises that need to be made for the shock compression seem to be as minor as in the case of the DAC usage.

- a) The radius of the vacuum chamber is somewhat larger (600 mm) than the one proposed by the DCS at the APS (500 mm) as far as we can tell from the very limited information we have. This was necessary in order to be able to drive the AGPID detector into the chamber to achieve good coverage of reciprocal space, something that the shock compression users will also benefit from. This also means that the equipment pre-aligned to the center of the chamber with a radius of the DCS chamber (500 mm) will have to be realigned to that of the DAC chamber (600 mm). According to the experts this will be possible and not too difficult.

- b) We are only able to offer fixed laser geometries of 22.5°, 45°, 67.5°, 90°, and 112.5° from the incident beam and the AGIPD detector can only cover a limited angular range of $\sim 2\theta = \pm 30^\circ$. However, since most of the experiments are done with PE XRD 4343 ct that can be rotated all around the chamber and cover large 2θ areas (see shock compression CDR for details) the limiting application of the AGIPD detector seems to be a minor draw back.

17. Time line and first experiments

Task	2015-A	2015-B	2016-A	2016-B	2017-A	2017-B	2018-A	2018-B
XFEL								
Electrons Injector	[Progress bar]							
First Electron in Undu.	[Progress bar]							
First Beam in SASE 2	[Progress bar]							
HED								
X-ray beam transport	[Progress bar]							
Infrastructure	[Progress bar]							
IA1	[Progress bar]							
First Beam at HED	[Progress bar]							
HIBEF								
Approved Funding	[Progress bar]							
Funding	[Progress bar]							
DAC Setup								
CDR	[Progress bar]							
DAC CDR @ SAC/TAC	[Progress bar]							
TDR	[Progress bar]							
DAC TDR @ SAC/TAC	[Progress bar]							
Construction	[Progress bar]							
1 st Exp. @ SAC/TAC	[Progress bar]							
First Experiments	[Progress bar]							
Detectors								
Detector Bench	[Progress bar]							
Perkin Elmer	[Progress bar]							
AGIPD (GaAs)	[Progress bar]							
Design	[Progress bar]							
Proto Type	[Progress bar]							
Construction	[Progress bar]							
First Experiments	[Progress bar]							



The time line for the DAC setup implementation is described above. Planning for the DAC setup at the HED will continue during 2016 and 2017. Construction can officially not start until 2018 when funding for HIBEF will become available.

18. Summary

In this document we have shown that high-pressure at simultaneous high-temperature diffraction experiments in the dDAC and dsDAC are possible and desirable to explore various scientific areas. In particular the exploration of the interior of exoplanets will be of significant interest to the planetary physics community. We have illustrated why these experiments cannot be performed at current and future 3rd generation light sources.

On the technical side we have shown how these types of experiments can be performed at the European XFEL and what might be the limitations. We have discussed the possibility to design a small vacuum chamber that will combine both DAC and laser shock experiments. We come to the conclusion that such efforts will result in only minor and tolerable compromises for the DAC setup.



19. References

- Anzellini *et al.* *Science* **340**, 464 (2013)
- Armstrong *et al.*, *J. Phys. Chem. A*, **117**, 13051-13058 (2013).
- Armstrong, *et al.*, *J. Appl. Phys.*, **108**, 023511 (2010).
- Beck *et al.*, *Appl. Phys. Lett.*, **91**, 181914.
- Belonoshko *et al.* *Nature* **424**, 10321034 (2003)
- Benedetti *et al.*, *Science* **286**, 100 (1999)
- Bini and Pratesi, *Phys. Rev. B* **55**, 22 (1997)
- Blome *et al.* *J. Syn. Rad.* **12**, 812 (2005)
- Boehler, *Nature* **363** 534536 (1993).
- Chen and Yoo, *PNAS* **108**, 7685 (2011)
- Chen and Yoo, *J. Chem. Phys.* **136**, 114513 (2012)
- Chen *et al.*, *J. Phys. Conf. Ser.* **500**, 142006 (2014a)
- Chen *et al.*, *Phys. Rev. B* **90**, 144104 (2014b)
- Cebulla and Redmer, *Phys. Rev. B* **89**, 134107 (2014)
- Coppari *et al.*, *Nat. Geosci.* **6**, 926929 (2013)
- Crowhurst, J.C., *et al.*, *Phys. Rev. Lett.*, **107**, 144302 (2011)
- Crowhurst, J.C., *et al.*, *J. Appl. Phys.*, **115**, 113506 (2014)
- Dalladay-Simpson *et al.*, *Nature* **529**, 63–67 (2016)
- Dewaele, *et al.*, *Phys. Rev. Lett.*, **104**, 255701 (2010)
- Dubrovinsky *et al.*, *Nat. Commun.* **3**, 1163 (2012)
- Dubrovinsky *et al.*, *Nature* **525**, 226–229, (2015)
- Dubrovinskaia *et al.*, *Scien. Advan.*, **2**, 1600341 (2016)
- Evans *et al.*, *Rev. Sci. Instrum.* **78**, 073904 (2007)
- Gilman, *Philos. Mag., Part B*, **71**, 1057-1068 (1995)
- Gorman *et al.*, *PRL* **115**, 095701 (2015)
- Guillot, *Science* **286**, 72 (1999)
- Hammersley *et al.*, *High. Press. Res.* **14**, 235 (1996)
- Hammersley, *ESRF Int. Rep.*, ESRF97HA02T (1997)
- Hirose, K., Lay, T., *Elements* **4**, 181 (2009)
- Jenie *et al.* in preparation (2016)
- Konôpková *et al.*, *Phys. Rev. B* **91**, 144101 (2015)
- Konôpková *et al.*, *Nature*, 534, 99-101 (2016)
- Kuppenko *et al.*, *Rev. Sci. Instrum.* **86**, 114501 (2015)
- Lobanov *et al.*, *J. App. Phy.* **118**, 035905 (2015)
- Lorenzen *et al.*, *Phys. Rev. Lett.* **102**, 115701 (2009)
- Lorenzen *et al.*, *Phys. Rev. B* **82**, 195107 (2010)



-
- Liermann, "X-Ray Diffraction at Extreme Conditions: Today and Tomorrow", In: X-ray Diffraction: Modern Experimental Techniques. Ed. Seeck & Murphy, Pan Stanford Publishing, 427 pp (2015)
 - Liermann et al., J. Synchrotron Rad. **22**, 908 (2015)
 - Loubeyre et al., Phys. Rev. B. **36**, 3723 (1987)
 - Loubeyre et al., PRL **71**, 2272 (1993)
 - Luo et al., Proc. Natl. Acad. Sci. U.S.A. **107**, 99624 (2010)
 - Marshall, Phys. Med. Biol. **54**, 2845 (2009)
 - McMahon et al. Rev. Mod. Phys. **84**, 1608 (2012)
 - McWilliams et al., Science **338**, 13303 (2012)
 - McWilliams et al., Phys. Earth Planet. Inter., 247, 17-26.
 - Morales et al. 2009, PNAS **106**, 1324 (2009)
 - Morales et al., Phys. Rev. B **87**, 174105 (2013)
 - Mundy et al., J. Chem. Phys., **128**, 184701 (2008)
 - Murakami et al., Science **304**, 855 (2004)
 - Narygina et al., Earth Planet. Sci. Lett. **307**, 409 (2011)
 - Nettelmann et al., Planet. Spac. Sci. **77**, 143 (2013)
 - Nellis *et al.*, J. Chem. Phys. **115**, 2 (2001)
 - Oganov et al., J. Chem. Phys. **118**, 10174 (2003)
 - Ping, Y. et al., PRL **111**, 065501 (2013)
 - Püstow et al., Icarus, in print (2016)
 - Prakapenka et al., High Press. Res. **28**, 225 (2008)
 - Prescher and Prakapenka, High Press. Res. **35**, 223 (2015)
 - Santamaria-Perez et al., Phys. Rev. B **81**, 214101 (2010)
 - Sakai et al. 2015, Rev. Sci. Instrum. **86**, 033905 (2015)
 - Schouten et al., Chem. Phys. Lett. **114**, 410 (1985)
 - Sinogeikin et al., Rev. Sci. Instrum. **86**, 072209 (2015)
 - Smith et al., Rev. Sci. Instrum. **86**, 072208 (2015)
 - Sun *et al.*, Chem. Phys. Lett. **473**, 72 (2009)
 - Tateno et al., Science **330**, 359361 (2010).
 - Tomasino and Yoo, App. Phys. Lett. **103**, 061905 (2013)
 - Tomasino et al., J. Chem. Phys. **140**, 244510 (2014)
 - Umemoto and Wentzcovitch, Earth Planet. Sci. Lett. **311**, 225 (2011)
 - Vocadlo, L. et al., Nature **424**, 536539 (2003)
 - Velisavljevic et al., J. Phys. Conf. Ser. **500**, 032020 (2014)
 - Weck et al., Phys. Rev. B, **76**, 054121.
 - White et al., Phys. Rev. Lett., **112**, 145005 (2014)
 - Whitley et al., J. Appl. Phys., **109**, 013505 (2011)
 - Wu et al., Phys. Rev. Lett. **103**, 065503 (2009)



- Zastra et al., Phys. Rev. E, **90**, 013104 (2014)

20. Appendix A:

Calculations of scattered flux in a Diamond Anvil Cell with a 0.02 mm thick sample of Iron on a Perkin Elmer Detector using Blome et al. (2005)

From Blome et al. 2005 we find for N_p = photons per pixel,

$$N_P = N_{hkl} \Delta(2\Theta)_{\text{pixel}} / \Sigma. \quad (1)$$

where N_{hkl} = integrated number of photons, Σ = width of the Bragg peak, and $\Delta(2\Theta)_{\text{pixel}}$ the angular size of the pixel. Here N_{hkl} is given by:

$$N_{hkl} = \frac{N_o \times T}{A} \left(\frac{e^4}{m_e^2 c^4} \right) \frac{V \lambda^3 m |F_{hkl}|^2}{4v^2} \frac{1}{\sin(\Theta)} \frac{\Delta y}{2\pi L \sin(2\Theta)} \quad (2)$$

Part 1
Part 2
Part 3
Part 4
Part 5

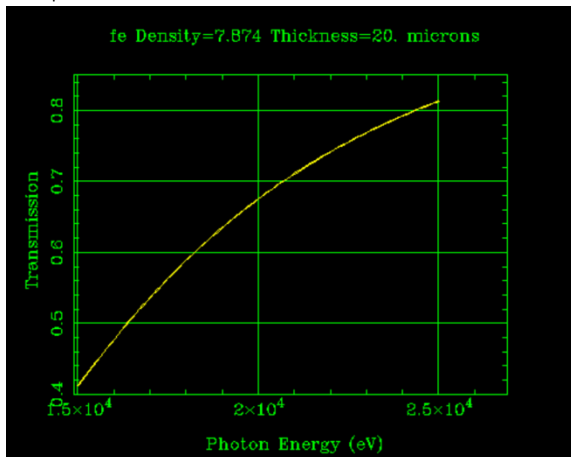
The values for the different parameters are as follows:

A) Part 1 (N_{eff} and Area)

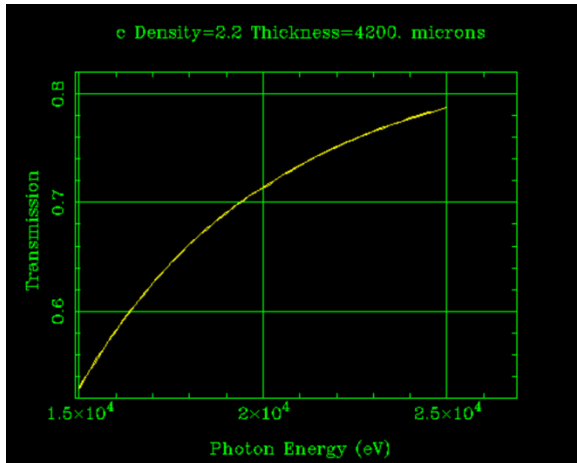
N_o = Number of incident photons and T = Transmission can be combined in $N_{\text{eff}} = N_o \times T$ = number of detectable photons

$T = T_{\text{sample}} T_{\text{Diamond}} T_{\text{air}} T_{\text{geo}} T_{\text{bw}}$ with

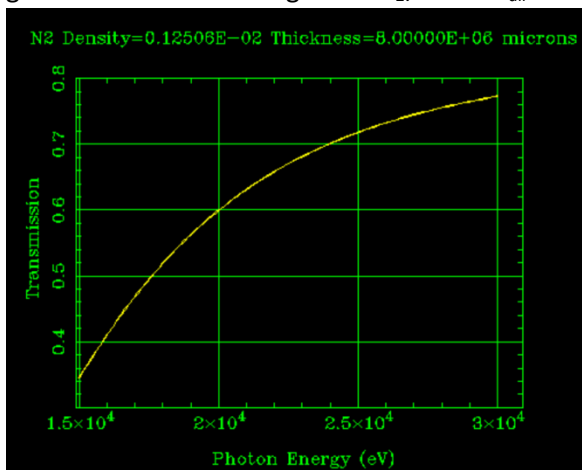
T_{sample} = transition due to sample absorption at 25 keV of a 0.02 mm sample of iron = 0.82



T_{Diamond} = transition due to diamond absorption at 25 keV of a $2.1 \times 2 = 4.2$ mm diamond (standard design with $x = 3.5$) = 0.78.



T_{air} = transition due to air absorption, which will be one since we are in vacuum = 1. However, for the sake of the argument, if you were to have a window at the entrance of the hutch (in order to have a not focused beam that can go through a diamond window) and you would let the beam run in air till it hits the sample one could estimate a total distance of ca. 8 m (estimated from the latest drawing I got from HED estimating air as N_2). Then $T_{\text{air}} = 0.78$.



T_{geo} = transition due to geometrical absorption which should be 1 since there is no restriction.

T_{bw} = transition due to bandwidth reduction which could be covered by varying the initial amount of flux.

Table 1: Calculations for N_p (photons per pixel) for Iron based on Blome et al. (2005).

Scenario	N_0 (ph/pulse)	T	N_{eff} (ph/pulse)	A (μm^2)	V (μm^3)	$IF^2 I_{(110)}$	θ (degrees)	$N_{(110)}$	N_p
25 keV ($\Delta E/E \ 10^{-3}$ $BW)_{\text{vac}}$	10^{12}	0.640	6.4×10^{11}	1	20	1401.943	7.027	3×10^5	2×10^5
				4	80	1401.943	7.027	3×10^5	2×10^5
				25	500	1401.943	7.027	3×10^5	2×10^5
				100	2000	1401.943	7.027	3×10^5	2×10^5
25 keV ($\Delta E/E \ 10^{-4}$ $BW)_{\text{vac}}$	10^{11}	0.640	6.4×10^{10}	4	80	1401.943	7.027	3×10^4	2×10^4

With the above values $T = T_{\text{sample}} T_{\text{diamond}} = 0.64$ and $T = T_{\text{sample}} T_{\text{diamond}} T_{\text{air}} = 0.461$. For different incident flux values (based on the bandwidth) you then find the value for N_{eff} listed in Table 1.

The variable A is the scattering area that depends on the beam size. We should use different beam sizes to be able to judge what we would lose if the beam size is larger and there would be less of a damage to the diamonds. Thus, I suggest 1, 2, 5, 10, 20 and 30 μm round size (FWHM), resulting in an area of $A = 1, 4, 25, 100, 400$ and $900 \mu\text{m}^2$.

B) Part 2

$$\frac{e^4}{m_e^2 c^4} = 7.94 \cdot 10^{-26} \text{cm}^2 = 7.94 \cdot 10^{-18} \mu\text{m}^2$$

C) Part 3 (Volume, Wavelength, multiplicity, unit cell volume, structure factor)

- The scattering volume is dependent on the scattering area and the thickness of the sample. Since we choose different beam size scattering volume is going to vary as well.

$$A = 1, 4, 25, 100, 400 \text{ and } 900 \mu\text{m}^2$$

$$\text{Thickness} = 20 \mu\text{m}$$

$$V = 20, 80, 500, 2000, 8000, 18000 \mu\text{m}^3$$

- $\lambda = \text{wavelength (25 keV)} = 0.4959 \text{ \AA}$

- $m = \text{multiplicity for the bcc iron for example (110) has a multiplicity of 12 (values for other reflection see in Table 2)}$

- $v = \text{unit cell volume for bcc iron} = (2.8665 \text{ \AA})^3 = 23.5412 \text{ \AA}^3 = 2.354 \cdot 10^{-11} \mu\text{m}^3$.

- $|F_{\text{hkl}}| = \text{structure factor of the hkl reflection} \Rightarrow \text{we will pick the structure factor of the (110) reflection.}$

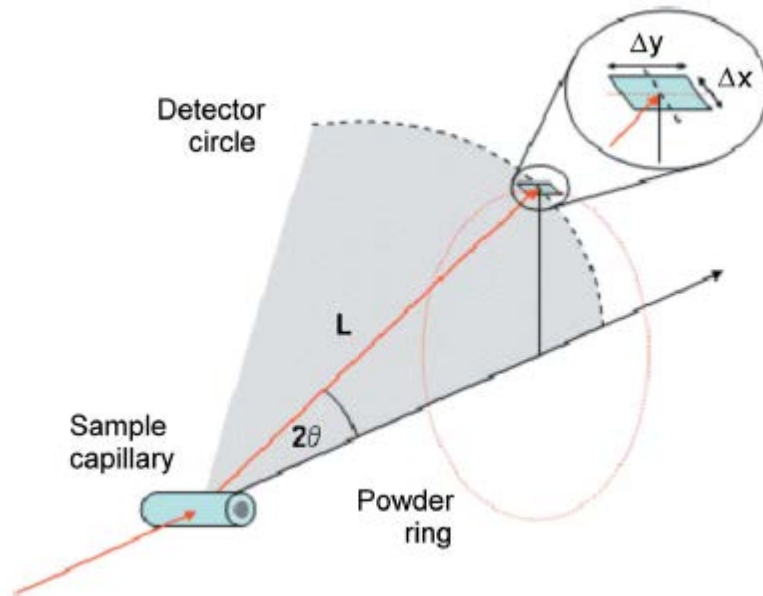
Attached are the necessary information on the multiplicity and the structure factor for iron bcc.

Space Group = $I m \bar{3} m$

Cell Parameter $a = 2.86650$

(hkl)	Multiplicity	$\text{Sin}(\theta)/\lambda$	2θ (degrees)	FWHM (degrees)	FWHM (mrad)	$ F^2 _{(\text{hkl})}$
110	12	0.24668	14.054	0.07460	1.3	1401.943
200	6	0.34886	19.926	0.07281		962.564
211	24	0.42726	24.467	0.07147		717.654
220	12	0.49336	28.325	0.07035		566.096
310	24	0.55159	31.752	0.06939		465.816
222	8	0.60424	34.875	0.06853		396.264

Table 2: Diffraction information for bcc iron, Space Group = $I m \bar{3} m$, Cell Parameter $a = 2.86650$ (from ...).



D) Part 4 and 5 (Diffraction Angle, SDD, pixel size)

- Diffraction angles are listed in table 2.
- The parameter L in formula (2) is dependent on the SDD which we assume to be a minimum of 300 mm, so that it becomes $L = SDD/\cos(2\theta) = 309.2569$.
- dy is related to illuminated area on the detector. Since the pixel size of the Perkin Elmer detector XRD1621 is 0.2 mm and we want to know how many photon one pixel will hit we approximate $dy = 0.2$ mm.

E) Np

From Formula (1) we can calculate the Np (photons per pixel). Here Σ = width of the Bragg peak in given in table 2 and $\Delta(2\theta)_{\text{pixel}}$ = angular size of the pixel can be calculated from $\text{tg}(2\theta_{+/-}) = \Delta \pm (dy/2) / SDD$ where $D = \text{tg}(2\theta) * SDD$ is the vertical distance at the SDD from the incident beam. The $\Delta(2\theta)_{\text{pixel}}$ (300 mm SDD) = $0.0359^\circ = 0.627$ mrad.